Journal Pre-proof

Physical controls of dynamics of methane venting from a shallow seep area west of Svalbard

A. Silyakova, P. Jansson, P. Serov, B. Ferré, A.K. Pavlov, T. Hattermann, C.A. Graves, S.M. Platt, C. Lund Myhre, F. Gründger, H. Niemann

Please cite this article as: Silyakova, A., Jansson, P., Serov, P., Ferré, B., Pavlov, A.K., Hattermann, T., Graves, C.A., Platt, S.M., Myhre, C.L., Gründger, F., Niemann, H., Physical controls of dynamics of methane venting from a shallow seep area west of Svalbard, *Continental Shelf Research*, https://doi.org/10.1016/j.csr.2019.104030.

This is a PDF file of an article that has undergone enhancements after acceptance, such as the addition of a cover page and metadata, and formatting for readability, but it is not yet the definitive version of record. This version will undergo additional copyediting, typesetting and review before it is published in its final form, but we are providing this version to give early visibility of the article. Please note that, during the production process, errors may be discovered which could affect the content, and all legal disclaimers that apply to the journal pertain.

1
2

Physical controls of dynamics of methane venting from a shallow seep area west of Svalbard

3   **A. Silyakova[a*], P. Jansson[a], P. Serov[a], B. Ferré[a], A. K. Pavlov[b], T. Hattermann[c,d], C. A.**
4   **Graves[e,f], S. M. Platt[g], C. Lund Myhre[g], F. Gründger[a] and H. Niemann[h,a,i]**

5   [a]CAGE - Centre for Arctic Gas Hydrate, Environment and Climate, UiT the Arctic University of
6   Norway in Tromsø, Department of Geosciences, Post box 6050 Langnes, 9037 Tromsø, Norway

7   [b]Norwegian Polar Institute, Fram Centre, Post box 6606 Langnes, 9296 Tromsø, Norway

8   [c]Akvaplan-niva AS, Fram Centre, Post box 6606, Langnes, 9296 Tromsø, Norway

9   [d]Alfred Wegener Institute, Helmholtz Centre for Polar and Marine Research, Am Handelshafen
10 12, D-27570 Bremerhaven, Germany

11 [e]Leibniz Institute for Baltic Sea Research Warnemünde, Seestrasse 15, D-18119 Rostock,
12 Germany

13 [f]Centre for Environment, Fisheries and Aquaculture Science, Pakefield Road, Lowestoft, Suffolk
14 NR33 0HT, UK

15 [g]NILU - Norwegian Institute for Air Research, Postbox 100, 2027 Kjeller, Norway

16 [h]University of Basel, Peterplatz 1, Postbox 4001, Basel, Switzerland

17 [i]NIOZ Royal Netherlands Institute for Sea Research, Department of Marine Microbiology &
18 Biogeochemistry, Postbox 59, 1790 AB Den Burg, Texel, the Netherlands

19 *Corresponding author: Anna Silyakova (**anna.silyakova@uit.no**), tel.:+4777644569

20 **Key words: Gas seepage; Water masses; Stratification; Multiyear variability; Methane**
21 **flux; Eddies; Ocean model; Svalbard shelf**

22

Abstract

We investigate methane seepage on the shallow shelf west of Svalbard during three consecutive years, using discrete sampling of the water column, echosounder-based gas flux estimates, water mass properties, and numerical dispersion modelling. The results reveal three distinct hydrographic conditions in spring and summer, showing that the methane content in the water column is controlled by a combination of free gas seepage intensity and lateral water mass movements, which disperse and displace dissolved methane horizontally away from the seeps. Horizontal dispersion and displacement of dissolved methane are promoted by eddies originating from the West Spitsbergen Current and passing over the shallow shelf, a process that is more intense in winter and spring than in the summer season. Most of the methane injected from seafloor seeps resides in the bottom layer even when the water column is well mixed, implying that the controlling effect of water column stratification on vertical methane transport is small. Only small concentrations of methane are found in surface waters, and thus the escape of methane into the atmosphere above the site of seepage is also small. The magnitude of the sea to air methane flux is controlled by wind speed, rather than by the concentration of dissolved methane in the surface ocean.

1 Introduction

The Arctic Ocean holds vast reservoirs of the potent greenhouse gas methane in the form of free and dissolved gas (Lammers et al., 1995; Damm et al., 2005), gas entrapped in subsea permafrost (Shakhova et al., 2010), and gas hydrates in sediments (Hester and Brewer, 2009; Westbrook et al., 2009; Berndt et al., 2014). In particular, gas that is bound in hydrates may be released as a result of temperature induced gas hydrate destabilization (Kretschmer et al., 2015; James et al., 2016), which makes the warming Arctic Ocean a potential hot spot of future methane emission (Shakhova et al., 2010; Kort et al., 2012; Parmentier et al., 2015). Methane release from the seafloor has been documented from numerous areas along the Arctic Ocean continental margin: the West Spitsbergen continental margin and shelf (Knies et al., 2004; Damm et al., 2005; Westbrook et al, 2009; Sahling et al., 2014; Smith et al., 2014; Graves et al., 2015; Mau et al., 2017), the Barents Sea (Lammers et al., 1995; Serov et al., 2017; Andreassen et al., 2017), the Kara Sea shelf (Portnov et al., 2013; Serov et al., 2015), the East Siberian Shelf (Shakhova et al., 2010, 2013), and the Beaufort Sea (Kvenvolden et al., 1993; Paull et al., 2007). Methane release from the West Spitsbergen margin particularly has been ongoing for several millennia and is, at least partly, temperature controlled (Berndt et al., 2014).

Indeed, Arctic air temperatures are increasing twice as fast as the global average because of Arctic amplification (Graversen et al., 2008; Serreze and Francis, 2006; IPCC 2014). The annual average Arctic air temperature is now 3.5°C warmer compared to the beginning of 20th century (Soreide et al., 2016). As a result, expanding areas of ice-free Arctic Ocean waters are being exposed to solar radiation and elevated air temperatures. Combined with an increase of heat input from adjacent ocean basins, e.g. warmer than usual Atlantic Water (AW) propagating deeper into the Arctic Ocean (Polyakov et al., 2004; 2007; 2010), this results in a present day Arctic Ocean sea surface temperature which is 5°C warmer than the 1982-2010 average for the Barents and Chukchi seas and around Greenland (Soreide et al., 2016). The effect of increasing temperature in the future Arctic may therefore become more important for Arctic seafloor methane liberation (Westbrook et al., 2009; Ferré et al., 2012; MarínMoreno et al., 2015).

66   Several processes determine the fate of methane released into the water column from
67 sediments and, most importantly, its release to the atmosphere. Methane contained in bubbles
68 emanating from the seafloor dissolves in seawater and can be rapidly transported from the area by
69 the advection of water masses (Graves et al., 2015). The upward transport of dissolved methane
70 has been found to be limited by water column stratification (e.g. Schmale et al., 2005; Leifer et
71 al., 2009). Studies by Myhre et al., (2016) and Gentz et al., (2014) conducted on the shallow shelf
72 and upper continental slope off Svalbard, west of Prins Karls Forland (PKF) revealed waters
73 enriched with dissolved methane below the pycnocline. However, the methane concentrations
74 above the pycnocline were generally in equilibrium with the atmospheric mixing ratio. This
75 suggested that the pycnocline may act as a physical barrier, preventing dissolved methane from
76 entering the well mixed upper layer of the water column and thus also the atmosphere, instead
77 trapping methane in the lower sphere of the water column. The open Arctic Ocean is stratified
78 throughout the year (Rudels et al., 1994). In shallower areas, however, the stratification of the
79 entire water column is subject to an annual cycle and a seasonal erosion of the pycnocline e.g.
80 through winter time convection or wind induced mixing (Cottier et al., 2010). If controlled by
81 stratification, the escape of methane to the atmosphere would also follow this seasonality. In
82 other words, the potential for methane to be liberated to the atmosphere from these areas is higher
83 when there is no stratification during stormy seasons (von Deimling et al., 2011).

84   Another important process determining the fate of methane in the water column is it's
85 removal by aerobic methane oxidation (MOx), mediated by aerobic methanotrophic bacteria
86 (Hanson & Hanson, 1996; Reeburg, 2007; Steinle et al., 2015). Methane removal from deep
87 water sources through MOx is more efficient than that from shallow sources, because the distance
88 between methane liberation from the seafloor and potential methane evasion to the atmosphere is
89 greater and methanotrophs in the water column have more time for methane consumption (Steinle
90 et al., 2015; Graves et al., 2015; James et al., 2016). For example, in the deep Gulf of Mexico
91 (~1500 meters water depth), most of the methane discharged following the Deepwater Horizon
92 oil spill was consumed by water column methanotrophs (Kessler et al., 2011), while most of
93 methane seeping from the shallow seafloor on the East-Siberian Shelf (~50 m water depth) was
94 liberated to the atmosphere, especially during storm-induced mixing events (Shakhova et al.,
95 2013).

96   Marine environments in the Arctic Ocean characterised by ongoing methane release are
97 ideal natural laboratories for studying the effects of potentially enhanced seafloor methane
98 venting in warming waters, and the processes that regulate the transport of this methane. In this
99 paper, we study the dynamics of methane venting from shallow gas-bearing sediments (water
100 depth: 50-120 meters) west of PKF off the Svalbard archipelago; and the physical processes in
101 the water column that control methane dispersion and displacement away from the seeps. We
102 conducted hydroacoustic surveys to determine the flux of free gas (i.e. bubbled methane) from
103 sediments, along with oceanographic surveys to determine concentrations of dissolved methane
104 in the water column, sea-air methane fluxes, and water mass properties. Measurements were
105 repeated in a defined study area during three consecutive years to investigate the dynamics of
106 venting methane under varying hydrographic conditions. Model simulations place these detailed
107 observations into the broader seasonal context, and allow a better understanding of the
108 oceanographic processes controlling methane dynamics in the area of study.

109

110 **2 Methods**

3

111
112   2.1 Study area

113   Our study area (423 km^2; 50 - 120 m water depth) is located west of PKF (Fig. 1). The
114 seafloor in this area is complex and characterized by abundant depressions and a sequence of
115 pronounced end moraine ridges: the Forlandet moraine complex (Landvik et al., 2005). Several
116 hundred methane flares were found during the present study and previous expeditions (e.g.
117 Sahling et al., 2014 and references therein). Similar to the adjacent shelf break, gas seepage is not
118 related to pockmarks or other fluid leakage related structures and the origin of the methane
119 remains unconfirmed (Westbrook et al., 2009; Berndt et al., 2014). Although hydrates have never
120 been recovered in the area and seismic evidence of gas hydrates is missing, sediment cores drilled
121 outside PKF contained freshwater presumably originating from dissociated gas hydrates
122 (Wallmann et al., 2018). Previous studies also suggest that free gas may originate from gas
123 hydrate dissociation deeper on the continental slope (>300 m) where gas hydrates have been
124 found (Sarkar et al., 2012) and migrate along the permeable zones towards the shelf (Westbrook
125 et al., 2009). An alternate hypothesis is that glacial rebound at the beginning of the Holocene
126 resulted in gas hydrate dissociation, which allowed for the formation of shallow gas pockets that
127 continue to release methane into the water column (Portnov et al., 2016; Wallmann et al., 2018).

128   The water masses and circulation in the study area are controlled to a large extent by the
129 interaction of coastal processes on the shelf with the West-Spitsbergen Current (WSC) that
130 circulates northward along the shelf break as the northernmost extension of the North-Atlantic
131 Current, transporting AW into the Arctic Ocean. The core of the WSC is at 250-800 meters water
132 depth (Perkin and Lewis, 1984) and the stream follows the slope of the continental margin
133 (Aagaard et al., 1987). By bringing large amounts of salt and heat, it affects the water column
134 structure in the entire area. Other currents in the area are the East Spitsbergen Current (ESC) that
135 advects Arctic waters into the region, and the coastal surface current, associated with the West
136 Spitsbergen Polar Front (Nilsen et al., 2016). Local scale physical processes affecting water mass
137 circulation include exchange of water masses between the WSC and shelf waters due to
138 instability of the WSC core and resulting eddies (Teigen et al., 2010; Hattermann et al., 2016;
139 Appen et al., 2016); as well as wind forcing and resulting upwelling events (Berge et al., 2005;
140 Cottier et al., 2007).
141

142   2.2 Survey design

143   We conducted research expeditions with the R/V Helmer Hansen in the study area during
144 three consecutive years: 25-27 June 2014 (hereafter, June-14), 01 – 03 July 2015 (July-15), 02 –
145 04 May 2016 (May-16). Each year we visited 64 hydrographic stations. Stations were positioned
146 in a grid for comprehensive coverage of the water column above active methane seeps (Fig. 1).
147 We collected hydrocast data from each station including continuous measurements of
148 conductivity, temperature, depth (CTD), and sampled the water column at discrete depths for
149 subsequent dissolved methane concentration measurements (see details in section 2.4). The entire
150 grid was subsampled within 3 days during each survey. Underway hydro-acoustic scanning of the
151 water column was performed to acquire information on gas flares (section 2.3). Ship-mounted
152 meteorological instruments continuously recorded air temperature, atmospheric pressure, wind
153 speed and direction. Furthermore, atmospheric methane mixing ratios were recorded
154 continuously with a Cavity Ring-Down Spectrometer (CRDS, PICARRO G2401) with an air
155 intake at 22.4 m above sea level.

156
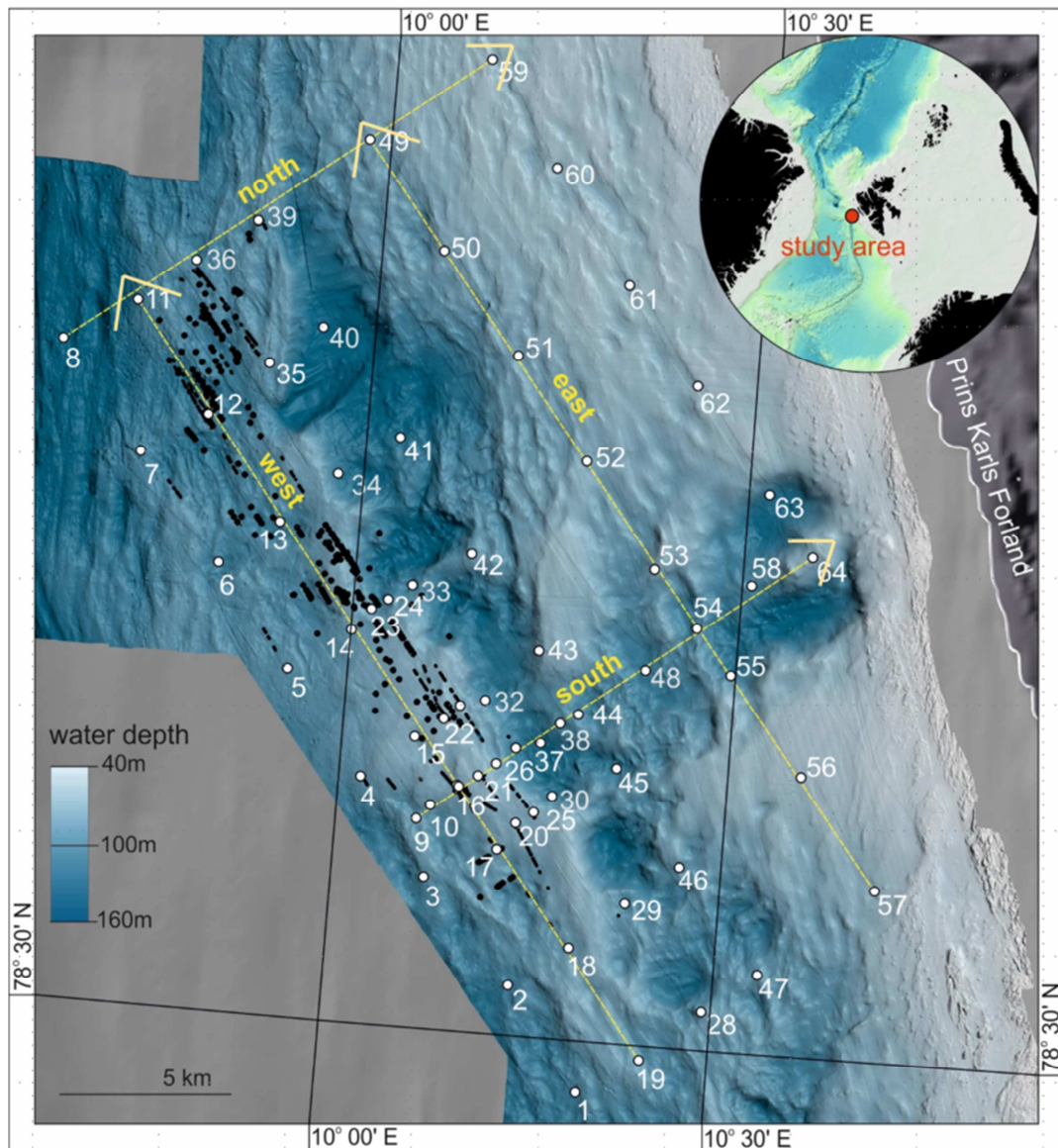
157
158
159 **Figure 1.** Bathymetric map of the study area with 64 hydrographic stations (white dots) for
160 oceanographic measurements west of the Svalbard archipelago (overview map). Black dots
161 indicate locations of methane seeps detected on echograms during all three surveys. Yellow
162 dashed arrows indicate transects shown in Fig. 4. Bathymetry data were acquired on board with a
163 Kongsberg Simrad EM 300 multibeam echo sounder (frequency of 30 kHz).

164

165   2.3 Hydroacoustic data acquisition and gas flux calculations

166

167   Gas bubbles in the water column were detected as acoustic signatures (flares) with a
168 Kongsberg Simrad EK60 single beam echosounder system. This system is primarily designed for
169 the fishery industry, but is also used to detect gas bubbles in the water column (Ostrovsky et al.,

170   2008; Nikolovska et al., 2008). Data were acquired at 38 kHz as this is the most appropriate
171   frequency to detect gas bubbles of sizes expected for cold seeps (Greinert et al., 2006). We used
172   the FlareHunter program (Veloso et al., 2015) to distinguish flares from other echo signals such
173   as fish, seafloor, and interference artifacts, and calculated flow rates from echosounder
174   backscatter based on beam compensated Target Strength (TS, dB) in a 5-10 meter layer above the
175   seafloor. We report free gas flow rates as mean values calculated from seven different bubble
176   rising speed models (BRSMs). The relative uncertainty between BRSM estimates is 16 %
177   (Veloso et al., 2015). The total length of our survey line was 408 km in June-14, 427 km in July-
178   15, and 300 km in May-16. Accounting for water depth and the resulting beam width radii of 5 –
179   20 m, the area of the seafloor investigated by the echosounder was 5.5 km^2 in June-14 and July-
180   15, and 3.8 km^2 in May-16, which amounts to ~1 % of the total study area. Since the fraction of
181   the study area covered by echosounder was small and slightly different between the three
182   surveys, we applied Kriging interpolation to scale up estimates over the entire study area and thus
183   facilitate comparison (details are provided in Supplementary material Text S1 and Fig. S1). Note
184   that Fig. 2 shows observed flow rates of single sources. For comparison with other studies we
185   present flow rates for the whole study area in Table 1 calculated as: (i) integrated over the entire
186   area volumetric flow rate (L min^{-1}); (ii) converted into mass flow rate (t y^{-1}) using the ideal gas
187   law and accounting for the average depth within each cell; and (iii) mean flux averaged over the
188   whole area (mmol m^{-2} d^{-1}), converted from mass flow rate using the molecular weight of methane
189   and divided by the survey area (423 km^2).

190   2.3 CTD profiling and water sample analyses

191   Vertical profiles of seawater temperature, salinity and pressure were recorded with a SBE
192 911 plus CTD probe at a rate of 24 Hz. The probe was mounted on a rosette including 12 5-litre
193 Niskin bottles. The Niskin bottles were closed during the up-cast (at speed of 1 m s^{-1}). For
194 analysis of hydrographic profiles, only down-casts were considered. Water samples were taken at
195 5, 15 and 25 meters above the seafloor and below the sea surface, and an additional two samples
196 were collected at evenly spaced depth levels between 25 m above the seafloor an 25 m below the
197 sea surface. In total, eight depths were sampled during all surveys.

198   Immediately upon recovery, sub-samples from the Niskin bottles were collected through
199 silicon tubing into 60 ml plastic syringes (June-14) or 120 ml serum glass bottles (Jule-15, May-
200 16) with rinsing by 2 – 3 overflow volumes. Syringes were closed with a 2-way valve and serum
201 bottles were crimp-sealed with butyl rubber septa. 5 ml N_2 headspace was added to the syringes
202 and serum bottles. Syringes/serum bottles with headspace were vigorously shaken for two
203 minutes to allow the headspace N_2 to equilibrate with the dissolved methane in the water sample.
204 Headspace methane mixing ratios were determined by gas chromatography (GC). During the
205 June-14 survey a ThermoScientific FOCUS GC equipped with a flame ionization detector (FID),
206 and a Resteck 2 m packed column HS-Q 80/100 with hydrogen (40 ml min) as a carrier gas was
207 used. During the July-15 and May-16 surveys a ThermoScientific Trace 1310 GC equipped with
208 an FID, and a Restek 30 m Alumina BOND/Na_2SO_4 column with hydrogen as a carrier gas (40
209 ml min^{-1}) was used. The column temperature was held constant at 40°C. The systems were
210 calibrated with external standards (2 ppm and 30 ppm in June-14 (Air Liquide); 10 ppm, 50 ppm,
211 and 100 ppm in July-15 and May-16 (Carbagas). Finally, water column methane concentrations
212 were calculated from headspace methane mixing ratios according to Wiesenburg & Guinasso
213 (1979) with consideration of salinity, sample temperature and ambient atmospheric pressure.

214   2.4 Calculations of water column methane content

215   To account for the uneven bathymetry (bottom depths of 50 to 120 m), when comparing
216 bottom, intermediate and surface waters, we divide the water column in three layers (Fig. S2): (1)
217 a bottom layer (0-15 meters above seafloor), (2) an intermediate layer (15 meters above seafloor
218 to 20 m water depth; the upper boundary roughly follows the depth of the pycnocline during the
219 July-15 survey, which we determined as a function of the Brunt–Väisälä frequency, see Fig. 5)
220 and (3) a surface layer (20 m water depth to sea surface). Detailed calculations of the methane
221 content (in mol) within the study area can be found in Supplementary material Text S2.

222   2.5 Calculations of the sea-air methane flux

223   The sea-air methane flux F (mol m^{-2} s^{-1}) was calculated according to Wanninkhof et al.
224 (2009):

225 $$F = k(Cw - Co), \text{ (Eq. 1)}$$

226 where k is the gas transfer velocity (m s^{-1}), Co is the methane concentration (mol m^{-3}) at the
227 ocean surface in presumed equilibrium with the atmosphere and Cw is the measured
228 concentration of methane (mol m^{-3}) in the well-mixed surface layer, typically measured at 5 m
229 water depth. The flux is positive and the ocean emits methane into the atmosphere if the

7

230 measured concentration in the surface layer is greater than the equilibrium concentration. *Co*
231 (mol m^{-3}) is defined as:

232
$$Co = \beta \, pCH_4, \text{ (Eq. 2)}$$

233 where β is the Bunsen solubility (mol m^{-3} atm^{-1}) of methane in seawater (Wiesenburg and
234 Guinasso, 1979):

235
$$\beta =$$
236
$$\exp[-68.8862 + 101.4956 \left(\frac{100}{T_W}\right) + 28.7314 \left[\ln\left(\frac{T_W}{100}\right)\right] + S\left(-0.076146 + 0.04397\left(\frac{T_W}{100}\right) - \right.$$
237
$$\left. 0.0068672\left(\frac{T_W}{100}\right)^2\right], \text{ (Eq. 3)}$$

238 where T_W is the water temperature (K) and S is the salinity.

239 pCH_4 is the partial pressure of methane in the air, derived from the mixing ratio of methane in the
240 atmosphere xCH_4 (mol mol^{-1}) measured by the on board CRDS at a height of 22.4 m (1902 ppb in
241 June-14, 1917 ppb in July-15 and 1955 ppb in May-16). The pCH_4 was calculated according to
242 Pierrot et al., (2009):

243
$$pCH_4 = xCH_4 * [P_{atm} - P_{wvapor}], \text{ (Eq. 4)}$$

244 accounting for the atmospheric pressure P_{atm} (atm) measured by the meteorological station on
245 board, and the water vapor pressure P_{wvapor} (atm) calculated according to Weiss and Price (1980):

246
$$P_{wvapor} = exp[24.4543 - 67.4509\left(\frac{100}{T_A}\right) - 4.8489\ln\left(\frac{T_A}{100}\right) - 0.000544S], \text{ (Eq. 5)}$$

247 where T_A is the air temperature (K) from the ships' meteorological station and S is the salinity of
248 spray in overlaying atmosphere, here assumed equal to the salinity of surface water.

249 The gas transfer velocity k is wind dependent and calculated as described in Graves et al. (2015)
250 and references therein:

251
$$k = 0.24 * u_{10}^2\left(\frac{Sc}{660}\right)^{-0.5}, \text{ (Eq. 6)}$$

252 where u_{10} (m s^{-1}) is the wind speed at 10 m above the sea surface, recalculated from the wind
253 speed u_{meas} (m s^{-1}) measured by the ships' anemometer at height 22.4 m (z_{meas}) after Hsu et al.,
254 1994:

255
$$u_{10} = u_{meas} * \left(\frac{z_{meas}}{10}\right)^{-0.11}, \text{ (Eq. 7)}$$

256 The Schmidt number Sc in Eq. 6 is the non-dimensional ratio of gas diffusivity and water
257 kinematic viscosity, and was defined as 677 in accordance with Wanninkhof et al., (2009).

258   2.6 Modelling of water mass properties and particle release experiments

259   To study seasonal variations in water mass properties and circulation and to scale up our
260 observations to a full year, we used a high-resolution regional ocean sea ice model. A more

261 detailed description and validation of the Svalbard 800 m horizontal resolution model (the S800-
262 model hereafter) can be found elsewhere (Albretsen et al., 2017; Hattermann et al., 2016; Crews
263 et al., 2017). Briefly, the S800-model provides hindcast ocean sea ice simulations for the
264 Svalbard and the Fram Strait region based on the Regional Ocean Modelling System (ROMS,
265 Shchepetkin and McWilliams, 2005) and a coupled sea ice component (Budgell, 2005). Boundary
266 conditions are provided by a 4 km pan-Arctic setup (A4-model). Bathymetry is based on the
267 ETOPO1 topography (Amante, 2009). Vertically, the model is discretized into 35 levels with a
268 layer thickness of less than 1 m near the surface over the continental shelf. The S800-model is
269 initialized and forced with daily averages from the A4-model, for which boundary conditions and
270 forcing fields are based on reanalyses (Storkey et al., 2010). Atmospheric forcing is provided by
271 ERA-interim reanalysis (Dee et al., 2011) and climatological river input from major rives in the
272 area, including freshwater runoff from the Svalbard archipelago (details in Hattermann et al.,
273 2016). The S800-model was initialized from January 2005, and the data shown in this study are
274 based on model runs from July 2005 to July 2010, averaged every month over that period.
275   Modelling results were extracted from a modelled field that included 41×56 grid points
276 and corresponded to the geographic area of the survey between CTD stations 1, 8, 57, 59, 64
277 (Fig.1; also red polygons in Fig. 10).
278   To investigate seasonal features of methane dispersion and displacement in the study area,
279 we conducted numerical experiments by simulative release of neutrally buoyant Lagrangian
280 drifters (hereafter particles) that were advected by the model velocity field. We released particles
281 from the polygon where the most intense seeps were observed during the surveys. The polygon
282 enclosed CTD stations 3 (113 m water depth), 4 (103 m water depth), 15 (91 m water depth), and
283 17 (97 m water depth) (Fig. 1). Due to varying water depths at these stations, we chose to release
284 particles from uniform depths between 80 and 100 m. Trajectories were computed using
285 Lagrangian particle tracking algorithm TRACMASS (Döös et al. 2017) based on the daily S800-
286 model output (see Hattermann et al. 2016 for details). Particles were released every day and were
287 tracked for a maximum lifetime of ten days. From the end positions of all particles released
288 within a respective month, histograms of particle distributions were computed by bin-counting
289 particle positions on the S800-model lattice. The histograms were normalized to the total number
290 of particles and used as a proxy for mapping the particle dispersion in the region. In addition,
291 monthly averages were computed according to the distance of particles from their source (as a
292 measure of the particle displacement) and to the distance from their mean position at t = 5 days
293 (particle dispersion).

294 **3 Results and discussion**

295   3.1 Controls on flare abundance and methane flux from sediments
296
297   We observed the densest flare cluster in the western and north-western part of the study
298 area (Fig. 2). This cluster was venting free gas during all cruises. In contrast, there was a
299 difference in flare density between surveys in the southern part of the study area, with the highest
300 flare density during the June-14 survey, and much lower densities during the July-15 and May-16
301 surveys. In total, we counted 225 individual flares in June-14, 208 in July-15 and only 92 during
302 the May-16 survey. The estimated gas flux from individual flares ranged between 20 and 600 ml
303 min^{-1} (Fig. 2). As a consequence of the decreasing flare density from June-14 to May-16, the
304 calculated total volumetric gas flow rate over the surveyed area was larger for June-14 (900 L
305 min^{-1}) than for the July-15 (665 L min^{-1}) and May-16 surveys (540 L min^{-1}) (Table 1).

9

306   We carefully checked for factors that may have potentially biased our estimates. The
307 May-16 survey was substantially shorter in distance (~70% compared to June-14 and July-15),
308 decreasing the confidence in scaling up our observations to the entire area. Yet, the western part
309 of the study area, where we always observed the highest flare density, was investigated during all
310 three surveys. Considering only this area, we could still identify a substantial decrease in both
311 flare density and volume flux. Consequently, artefacts from the scaling up the observations made
312 during surveys of different distance cannot explain the observed differences in seepage activity.

313   Temporal variability in the activity of seafloor methane seeps has been reported
314 previously (e.g. Greinert et al., 2006; Klaucke et al., 2010; Kannberg et al., 2013). Römmer et al.
315 (2016) investigated a cold seep offshore Canada at 1250 m water depth and suggested that the
316 pressure change of 1.9 dbar between low and high tide affected seepage activity with increasing
317 gas flux during falling tides. However, our survey period lasted for ~3 days, i.e. ~6 tidal cycles,
318 so that potential forcing by tides should be equalised and tides cannot be the reason for
319 differences in seepage activity between the surveys.

320   Variability in gas flux in our study area (highest in June-14, lower in July-15 and lowest
321 in May-16) follows observed between-survey differences in bottom water temperature (Fig. S3).
322 This was highest in June-14 (3.63±0.2°C), lower in July-15 (3.49±0.2°C) and the lowest in May-
323 16 (1.77±0.1 °C). Indeed, it has been proposed that seasonal fluctuations in bottom water
324 temperature modulate seepage activity off Svalbard, but from gas hydrate bearing sediments at
325 the termination of the gas hydrate stability zone (Berndt et al., 2014). However, gas hydrates have
326 never been found in our study area, which is at ~200 m shallower water depth than that of gas
327 hydrate stability limit (>300 m water depth), so that we can only speculate about the mechanisms
328 of a potential temperature control on seepage activity. Nevertheless, potentially modulating
329 effects of bottom water temperature would imply seasonal fluctuations in seepage activity in our
330 study area.

331

332
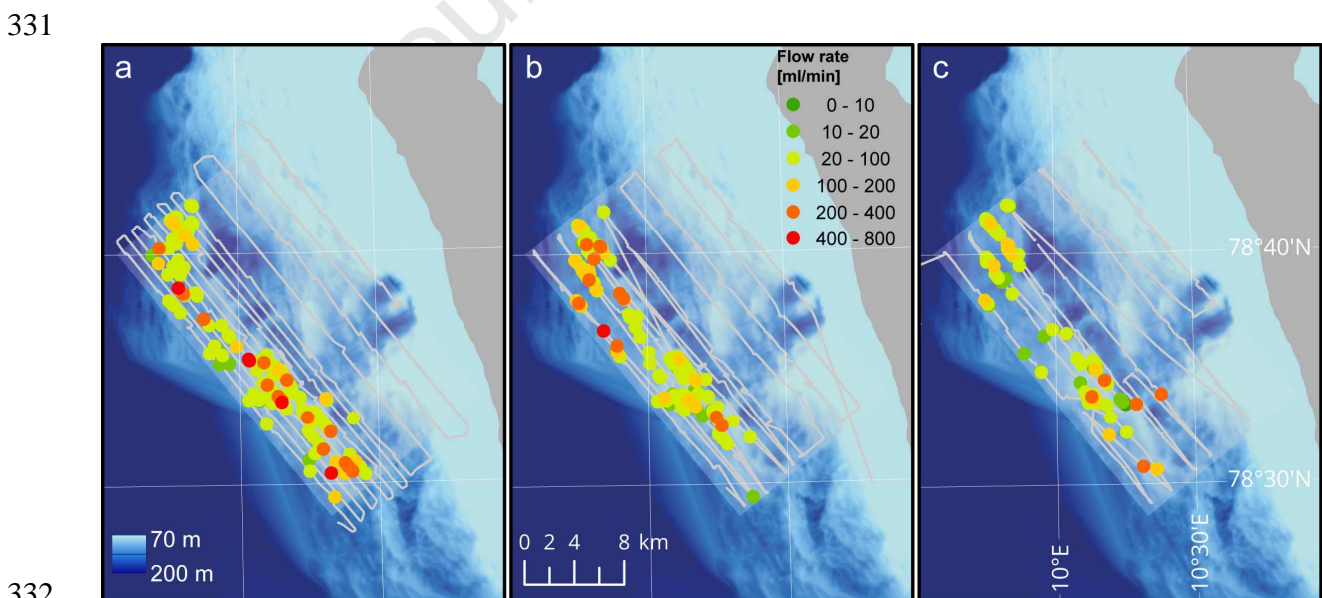
333
334 **Figure 2.** Flow rates from single sources (flares) during June-14 (**a**), July-15 (**b**) and May-16 (**c**)
335 surveys. Coloured circles indicate gas flow rates in ml min^{-1} from individual flares on the
336 seafloor. The grey line represents the ship track and echosounder beam coverage.
337

338 **Table 1.** Methane fluxes from sediments in different surveys

Survey	Total volumetric flow rate in the area (L min^{-1})	Total mass flow rate in the area (t y^{-1})	Average methane flux from sediments (mmol m^{-2} d^{-1})
June-14	899	3774	1.53
July-15	665	3004	1.21
May-16	542	2356	0.96

339 3.2 Controls of sea-air methane flux

340 The highest sea-air methane flux of 15 μmol m^{2} d^{-1} was observed during the June-14
341 survey, a lower flux of 11 μmol m^{2} d^{-1} was observed in July-15, and the lowest flux of only 2
342 μmol m^{2} d^{-1} was observed during the May-16 survey (Fig. 3 d-f). The temporal pattern of
343 atmospheric methane mixing ratios was the opposite of that of the flux, i.e. we found the lowest
344 mixing ratios in June-14 (1902 ± 0.52 ppb), higher during the July-15 (1917 ± 3.30 ppb) and the
345 highest during the May-16 survey (1955 ± 25.4 ppb) (data given as average ± standard deviation
346 of all observations during each survey). Thus, the atmospheric mixing ratio of methane was one
347 of the main controls on sea-air fluxes resulting in a supressed flux in case of higher atmospheric
348 methane values (e.g. lower fluxes in May-16 compared to the highest encountered atmospheric
349 methane mixing ratios). A further key control on sea-air methane fluxes is the concentration of
350 methane in the well-mixed surface waters, which was 9 nmol L^{-1} in June-14, and 3 nmol L^{-1}
351 during the July-15 and May-16 surveys (Table 2). Despite the similar surface water
352 concentrations in July-15 and May-16, sea-air methane fluxes were 5 times higher in July-15 than
353 in May-16. This can be explained by the wind speed, which was comparably low and varied very
354 little during the June-14 (4-8 m s^{-1}) and May-16 surveys (1-6 m s^{-1}), but increased from calm 4-6
355 m s^{-1} to strong 10-12 m s^{-1} towards the end of the 3-day July-15 survey (Fig. 3b). Generally, the
356 differences between the atmospheric methane mixing ratio and surface water methane content as
357 well as wind speed determine the variation in average sea-air flux. However, we argue that wind
358 speed plays the most important role in our study area with respect to sea-air methane fluxes. High
359 wind speeds can intensify efflux to the atmosphere even if the surface water methane
360 concentration is relatively low as long as the surface waters are supersaturated with respect to the
361 atmosphere.

362 To further test how the wind speed affects sea-air methane flux, we determined what the
363 flux would have been if the wind speed had been a 5 m s^{-1} throughout all surveys. In other words,
364 we used the observed values of surface water methane concentrations and atmospheric methane
365 mixing ratios measured during each survey, but instead of the measured wind data, we calculated
366 fluxes for a constant wind speed of 5 m s^{-1}, which is the climatological average wind speed for
367 late spring to early summer in our study area (The Norwegian Meteorological Institute,

11

368   www.yr.no). The meteorological mean was lower than the measured wind speed in June-14 and
369   July-15, but higher than the measured wind speed in May-16. Therefore, our flux calculations
370   with the mean values produced lower flux values for the June-14 (10 μmol m^2 d^{-1}) and July-15 (4
371   μmol m^2 d^{-1}) surveys, but higher values for the May-16 (3.5 μmol m^2 d^{-1}) survey (Fig. 3 g-i). This
372   comparison between sea-air methane flux with actual measured and constant wind speeds
373   highlights the importance of wind speed in modifying methane emission to the atmosphere in our
374   study area.

375

376
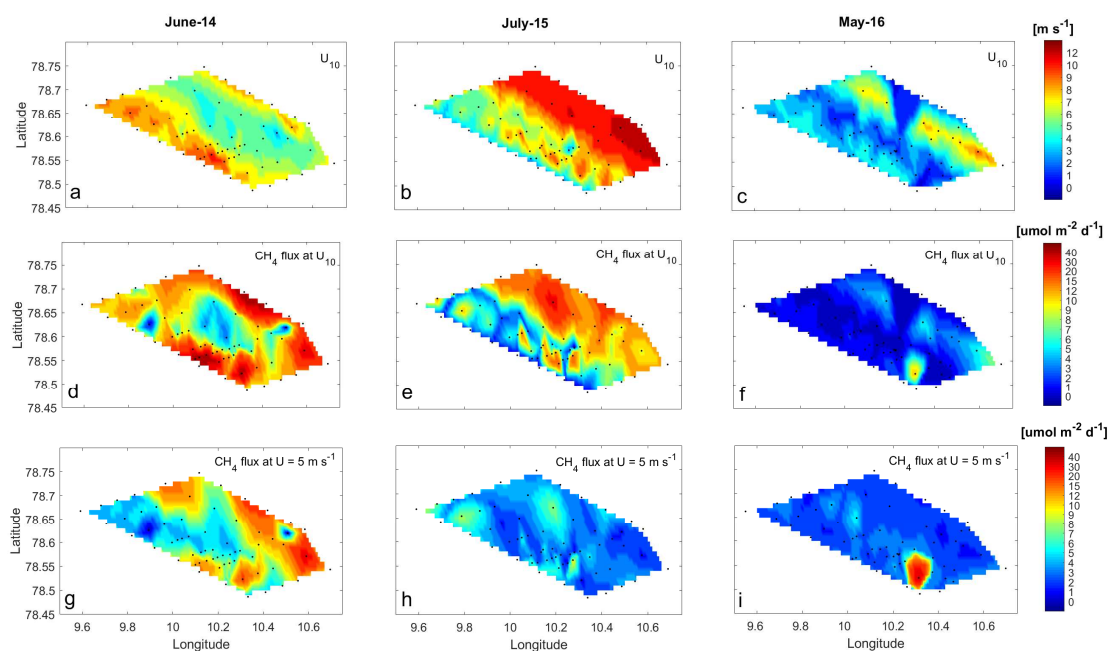
Figure 3. Wind speed measured at 22.4 m above sea level (upper panel: **a**, **b**, **c**), Methane flux at
the air-sea interface at measured wind speed u_{10} (mid panel: **d**, **e**, **f**) and methane flux at the air-
sea interface at constant wind speed U=5 m s^{-1} for May-July (lower panel: **g**, **h**, **i**), for the entire
grid and the three surveys.

381   3.3 Controls of water column methane content
382

383   The water column above active methane flares in the study area was divided into three
384   layers in order to estimate differences between methane content in the bottom 15 m, where
385   presumably most of released methane dissolves; the surface 20 m which roughly corresponds to
386   the thickness of the well mixed surface layer in summer and from which outgassing most of
387   methane to the atmosphere occurs; and the intermediate layer between the bottom and surface
388   layers, which is the thickest and presumably accumulates most of the released methane. When
389   comparing different layers, the highest methane concentrations were found in bottom layer as
390   expected. However, in all surveys the overall highest methane content was found in the
391   intermediate layer because it contains the highest volume of water (extends through the largest
392   depth interval). When comparing different surveys, we observed the highest total methane
393   content in June-14 (23×10^5 mol), lower in July-15 (15×10^5 mol) and lowest during the May-16
394   (14×10^5 mol) survey (Table 2).

395

396 **Table 2**. Average dissolved methane concentrations and content in different layers during each
397 survey

Layer → Survey ↓	Surface (surface-20 m water depth)	Intermediate (variable depth depending on water depth)	Bottom (bottom-15 m above the bottom)	Total
Average methane concentrations (nmol L^{-1})				
June-14	9.4	55.4	92.3	
July-15	3.1	31.9	70	
May-16	3.2	26.6	61.3	
Average content (×10^{-3} mol m^{-2})				
June-14	0.17	3.79	1.39	5.35
July-15	0.06	2.36	1.04	3.46
May-16	0.07	2.32	0.91	3.30
Total content in the surveyed area (×10^{5} mol)				
June-14	0.73	16	5.87	23
July-15	0.26	10	4.40	15
May-16	0.28	9.8	3.85	14
Total mass of methane in the surveyed area (t)				
June-14	1.17	25.73	9.41	36.31
July-15	0.43	16.00	7.05	23.50
May-16	0.44	15.77	6.17	22.38

398   The change in dissolved methane content in the water column between the surveys is
399 similar to the trend in the number of observed flares and the volume of released gas, and, to a
400 smaller extent, the sea-air methane flux. Although the correlation between the amount of released
401 methane and its content in the water is anticipated, there are number of processes that we did not
402 measure, some of which could alter the methane content in the entire water column, and some, in
403 surface waters alone.

404   One of these processes is aerobic methane oxidation (MOx), which leads to methane
405   undersaturation of deep waters in the entire ocean (Reeburgh, 2007). During MOx, methane is
406   removed from the water column when it is consumed by bacteria who use methane as a source of
407   carbon and energy. To test how important the role of MOx is in the removal of methane from the
408   system, we used MOx rates reported for the regions near our study area. Gentz et al. (2014)
409   reported MOx rate of 0.8 nmol L^{-1} d^{-1} in bottom waters and 0.2 in surface waters in the water
410   column above methane flares with absolute depth of ~250 m, while Steinle et al. (2015) found
411   higher rates of 2 nmol L^{-1} d^{-1} in bottom water alongside lower rates of only 0.1 nmol L^{-1} d^{-1} in
412   surface waters above methane flares with an absolute water depth of 360 m. After vertical and
413   horizontal integration of these estimates over our area, we found that less than 10% of the
414   released methane in our study area per day is likely to be removed from the system through MOx,
415   suggesting that this process does not play a major role in the removal of methane injected from
416   sediments at this site.

417   Another process mediating methane content in the water column is aerobic methane
418   production by microbes under phosphorus limiting conditions (Karl et al., 2008). In the oceanic
419   interior, this process leads to methane supersaturation in the surface water column above the
420   pycnocline (Reeburgh, 2007). Such methane supersaturation in surface waters was found in the
421   Fram Strait to the west from our study area, but only reached maximum concentrations of 9 nM
422   at 10-20 m depth (Damm et al., 2015). We observed only one case of isolated high surface
423   methane concentration (of 20 nmol L^{-1}) during the June-14 and May-16 surveys, but in most
424   cases surface concentrations were close to atmospheric equilibrium, thus we assume that in our
425   study area the methane contribution from this process is of low importance.

426   These two biological processes are important on the scale of entire ocean but are minor
427   mediators of methane content in our study area which experiences rapid methane injection into
428   the system at the seabed and methane concentrations hundreds of times higher than the average
429   oceanic concentrations. For example, considering a total injection of methane from sediments of
430   5.2×10^5 mol d^{-1} (averaged over the three surveys), a loss through sea-air gas exchange of $0.04 \times$
431   10^5 mol d^{-1}, and a MOx rate of 0.58×10^5 mol d^{-1} (based on estimates from Gentz et al. (2014)
432   and Steinle et al. (2015) for nearby waters), the resulting amount of methane in the water column
433   would be 4.6 mol $\times 10^5$ mol d^{-1}. Our total methane content averaged over the three surveys is $17 \times$
434   10^5 mol, which is 3.8 times higher than the resulting content, implying a residence time of
435   methane in the study area of about 3.8 days. However, methane is likely transported beyond our
436   survey area during this time through transport by lateral water movement (section 3.5). To see
437   how efficient this transport is and what affects it in our study area, we look further into vertical
438   and horizontal distribution of methane in different surveys.

439   3.4 Controls of the vertical distribution of dissolved methane
440
441   Highest dissolved methane concentrations were found in the bottom layer (> 300 nmol L^{-1})
442   in the south-western part of the sampling area during all three surveys (Figs. 4d-i, 4d-i). Waters
443   supersaturated with methane were found around flares from the seafloor up to 50 (July-15) and
444   20 meters water depth (June-14, May-16). Methane supersaturated waters have methane
445   concentrations > 3.7 nmol L^{-1}, which would be in equilibrium with the atmosphere for a salinity
446   of 35 at 0° C and atmospheric mole fraction of methane 1.9 ppb (average value for all three
447   surveys) (Wiesenburg and Guinasso, 1979). In all three surveys, the intermediate layer methane

448 concentration averaged over the entire area was only half of the bottom layer concentration, while
449 the surface water concentrations were 25 times lower than the bottom layer concentrations.


450
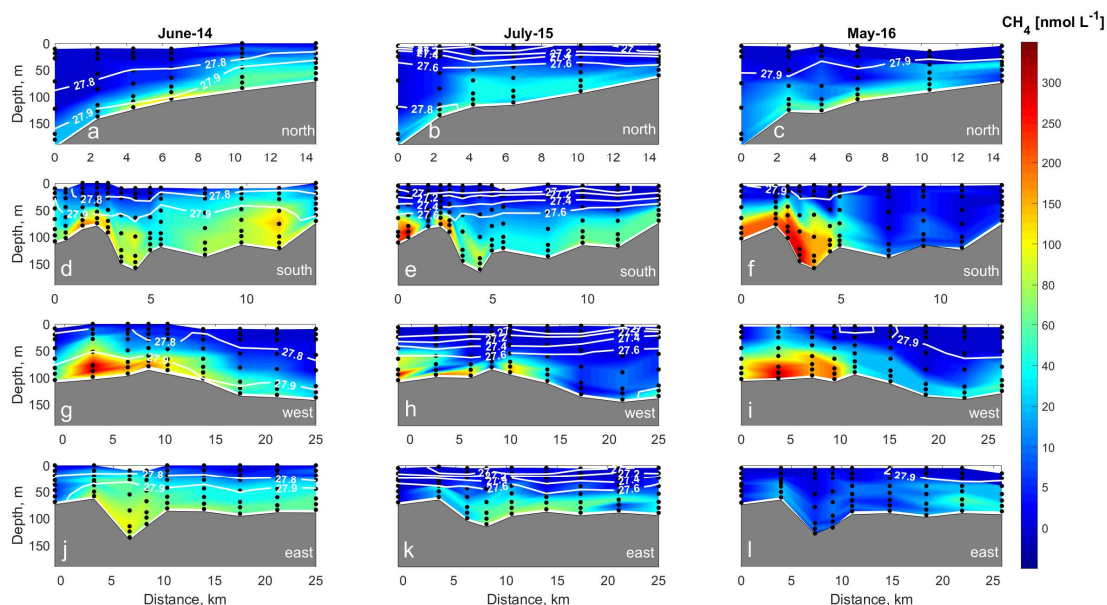
Figure 4. Distribution of dissolved methane along four transects (north (**a**, **c**, **d**), south (**d**, **e**, **f**),
452 west (**g**, **h**, **i**) and east (**j**, **k**, **l**); c.f. Fig. 1 for location and direction of each transect. Seawater
453 density (in kg m^{-3}) is indicated by white contour lines. Locations of discrete samples for methane
454 concentration measurements are indicated by black dots.

455   Our results show methane enriched bottom and intermediate waters, and surface water
456 which are only slightly supersaturated or close to atmospheric equilibrium. These results agree
457 well with earlier measurements near our study area (e.g. Gentz et al., 2014; Westbrook et al.,
458 2009; Mau et al., 2017), which showed high methane concentrations in bottom waters above
459 methane flares, and rapid decreases in methane concentrations towards the surface. This pattern
460 in vertical distribution can be explained by ongoing gas exchange between rising methane
461 bubbles and the surrounding seawater (e.g. McGinnis et al., 2006). This leads to continuous
462 replacement of methane in the bubbles with N_2 and O_2 from the seawater and methane
463 enrichment of seawater along the bubble ascent. Modelling approaches suggest that the bulk of
464 methane is already stripped out from rising bubbles close to the seafloor, so that bottom waters
465 become more enriched with dissolved methane (McGinnis et al., 2006). Bubbles observed close
466 to the surface are thus mostly comprised of N_2/O_2. Only bubbles of >20 mm in diameter may still
467 contain 1% of their initial methane content at the surface, but such bubbles typically break apart
468 during their ascent (McGinnis et al., 2006).

469   Vertical transport of dissolved methane that has already escaped bubbles has been
470 proposed to be limited by water column vertical stratification, when a pycnocline acts as a barrier
471 for vertical mixing of methane rich waters in strongly stratified waters (Gentz et al., 2014; Myhre
472 et al., 2016). As a proxy for water column vertical stratification, we calculated the Brunt–Väisälä
473 frequency (N^2) in our study area (Millard et al., 1990), which generally peaked at ~20m water
474 depth, and was the highest in July-15 (4×10^{-4} s^{-2}), ~8 times lower during the June-14 survey

475   (0.5×10^{-4} s^{-2}) and near zero in the entire water column during the May-16 survey (0.1×10^{-4} s^{-2})

476   (Fig. 5c). In July-15 the observed strong stratification was formed by a temperature drop from 5.5

477   °C at the surface to 3.5°C at 50 m water depth forming pronounced thermocline (Fig. 5a); and by

478   a salinity increase from 34.1 at the surface to 34.9 at 100 m depth along a continuous halocline

479   (Fig. 5b). Conversely, in May-16 the water column was well-mixed, with almost uniform

480   temperature and salinity with depth, and the near- absence of a pycnocline.
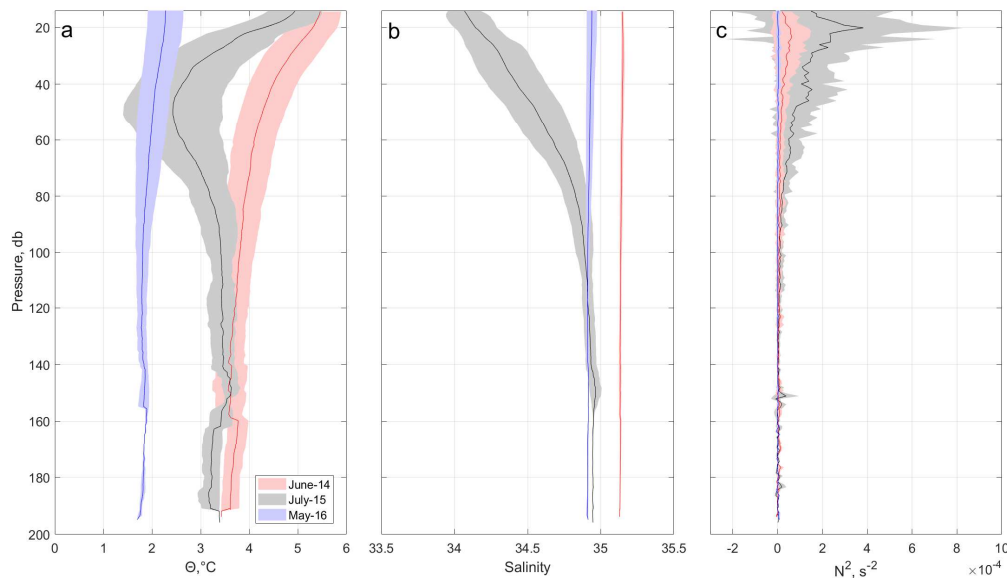
481

482   **Figure 5.** (**a**) Potential temperature (Θ, °C), (**b**) salinity and (**c**) Brunt–Väisälä frequency

483   (N^2, s^{-2}) averaged over all CTD stations for each survey with standard deviation shown as shaded

484   error bars. Colours indicate: June-14 (red), July-15 (black) and May-16 (blue).

485   Despite the difference in stratification between the three surveys (Fig. 5c), the vertical

486   distribution of dissolved methane (high bottom water methane concentrations and low surface

487   water concentrations) was similar across all three surveys (Fig. 4). This indicates that methane

488   released from the sediments and dissolved in seawater did not rise above 20-50 m water depth

489   towards the sea surface, even in the absence of a pycnocline. Our findings thus suggest that water

490   density stratification may not always play the principle role in the vertical distribution of

491   dissolved methane in cold seeps areas, in contrast to the conclusions of previous studies in this

492   area (Myhre et al., 2016: Gentz et al., 2014). Furthermore, our results do not show an influence of

493   stratification on water column methane content or the sea-air gas flux.

494   3.5 Controls of horizontal distribution of dissolved methane

495   The horizontal distribution and patchiness of methane differed between the three surveys.

496   During the June-14 survey we observed elevated dissolved methane concentrations in the bottom

497   and mid-depth layers (Fig. 6d and g) spread over the entire survey area. In contrast, during May-

498   16, methane concentrations were high (up to 400 nmol L^{-1}) only above flares clustered in the

499   south-western part of the area, and decreased considerably to < 40 nmol L^{-1} within a few hundred

16

500   meters away from the flares (Fig. 6i). Elevated methane concentrations also spread horizontally
501   in July-15, but to a lesser extent than during the June-14 survey.

502   In the surface layer, methane concentrations were generally low and near the atmospheric
503   equilibrium (Fig 6a-c). Some elevated surface methane concentrations (~20 nmol L^{-1}) were
504   observed at one station in the southeast part of the study area in June-14 and in the south-western
505   part of the study area during the May-16 survey.
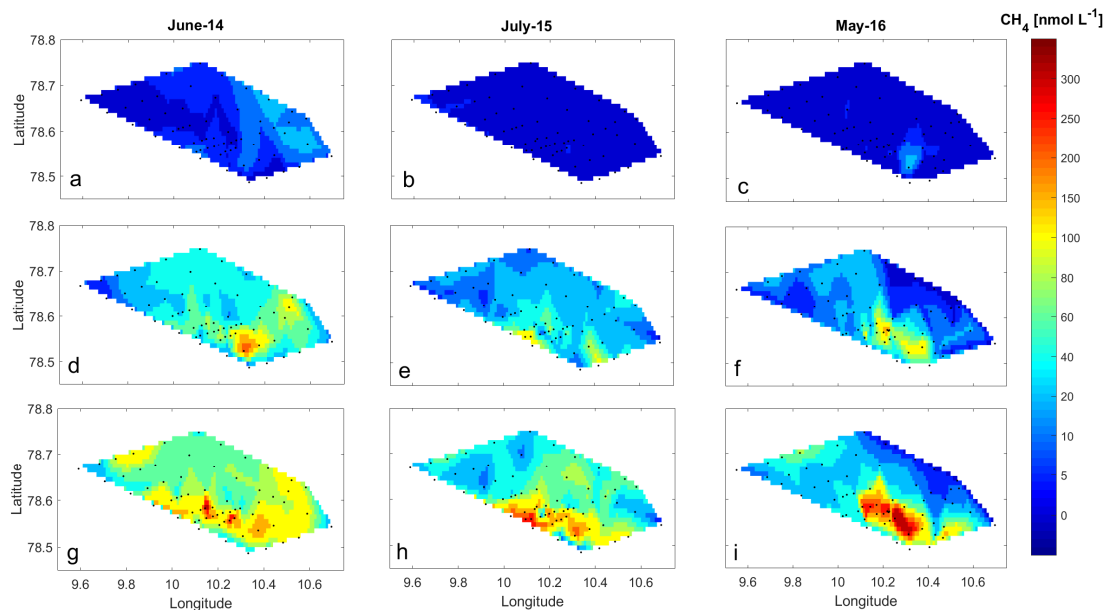
506

507   **Figure 6.** Average methane concentrations in the surface (0-20 m, **a**, **b**, **c**), intermediate (20 m –
508   15 m from the seafloor, **d**, **e**, **f**) and bottom water (within 15 m of the seafloor, **g**, **h**, **i**), layers for
509   the entire grid during the three surveys as indicated above the figures.

510   High variability in water mass properties indicates that circulation during all surveys was
511   controlled by several factors. We used the classification of water masses suggested by Cottier et
512   al. (2005) for Svalbard fjords and adjacent shelf regions to describe the oceanographic setting in
513   our study area. During the June-14 survey we observed only warm and saline AW (temperature Θ
514   >3°C, absolute salinity S_A >34.65) (Fig. 7a), brought to the study area with the WSC. In contrast,
515   water in July-15 was substantially colder and less saline (Fig. 7b), mainly comprised of AW, with
516   some Transformed Atlantic Water (TAW, $1 < \Theta < 3$°C, S_A >34.65), and to the largest extent,
517   Intermediate Water (IW, Θ >1°C, $34 < S_A < 34.65$). IW originates from fjords and forms as AW
518   that cools over winter in fjords, and is freshened by glacial melt, sea ice melt and river runoff
519   during summer. IW can also be a mix of AW and Arctic Water masses (ArW, $-1.5° < \Theta < 1$°C,
520    $34.3 < S_A < 34.8$) transported from the Northern Barents Sea around southern tip of Svalbard
521   with the ESC. During the May-16 survey (Fig. 7c), the water column mainly comprised TAW
522   with absolute salinity values similar to AW but with potential temperatures around $1.5 – 3$°C,
523   which is colder than the typical AW with temperature defined as above 3°C. There was a strong
524   presence of AW on the shelf and adjacent fjords in 2016 (F. Nilsen, pers. comm.). The core of the
525   AW in May is always above 2.5°C (Beszczynska-Möller et al., 2012). Our measured colder

526 seawater temperatures in the area could indicate that AW was cooled by the atmosphere or
527 surrounding waters, either locally or before it was advected from adjacent basins.
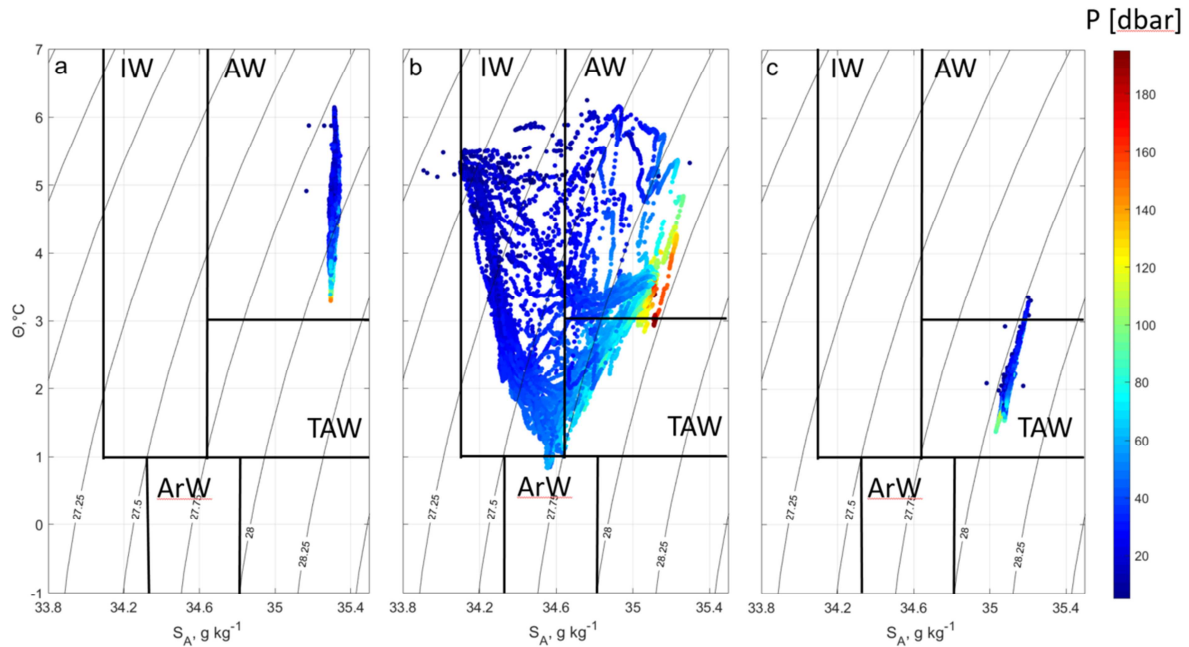

528

529 **Figure 7.** Potential temperature (Θ, °C) – absolute salinity (S_A, g kg^{-1}) diagrams for the June-14
530 (**a**), July-15 (**b**) and May-16 (**c**) surveys. Θ, °C calculated according to the International
531 Thermodynamic Equation of Seawater (Fofonoff and Millard, 1983). Absolute salinity calculated
532 based on measured practical salinity, and is expressed in terms of g of salt per kg of water. Grey
533 contours indicate isopycnals (kg m^{-3}).

534 Seawater temperature and salinity modelled with the S800-model (Hattermann et al.,
535 2016) for the study area indicate a shift from AW to IW properties towards summer and autumn
536 months due to surface warming and freshening (Fig. 8), hence revealing the annual cycle of water
537 mass formation. Salinity shows a seasonal cycle only at the surface, where it decreases from 35 in
538 June to 34.4 in September (Fig. 9). Summer freshening of the surface results from freshwater
539 runoff from land, glacial and sea ice melt, and a varying presence of ArW in the study area.
540 Bottom water salinity of about 35 is constant throughout the year, such that the seasonal cycle of
541 density near the seafloor is controlled by temperature. Surface and bottom water temperatures
542 rise towards summer, following atmospheric temperatures, regardless of which water mass is
543 present in the area (Fig. 9). Temperatures increase towards summer from 2.5 to 6°C at the
544 surface, and from 1.5 to 4°C at the bottom. The maximum temperature in the surface water is
545 observed in July-August and one month later near the bottom. Winter surface and bottom
546 temperatures vary between 1.5 and 2.5°C indicating that the water column is cooled down by
547 heat loss to the atmosphere or surrounding waters (Nilsen et al., 2016). Warming of the water
548 column in the study area throughout the year occurs through intermittent heat exchange with the
549 WSC that floods the shallow shelf (Nilsen et al., 2016), likely in a form of baroclinic eddies,
550 which are abundant in this region (Appen et al., 2016, Hattermann et al., 2016).

551
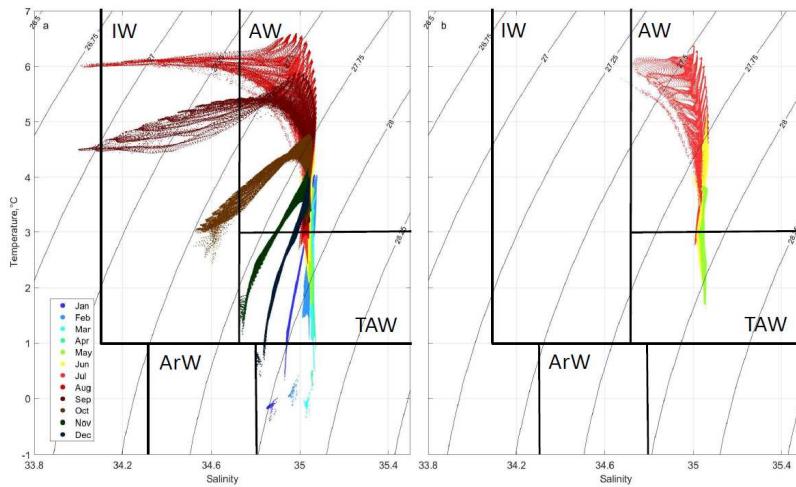
Figure 8. TS diagrams based on S800-model data for the study area, monthly average over the
period July 2005 – July 2010 (**a**); monthly average in May, June and July as these months are
when the surveys were conducted (**b**). Colours indicate month of the year as shown in the legend.
Background contour lines show isopycnals (kg m^{-3}).
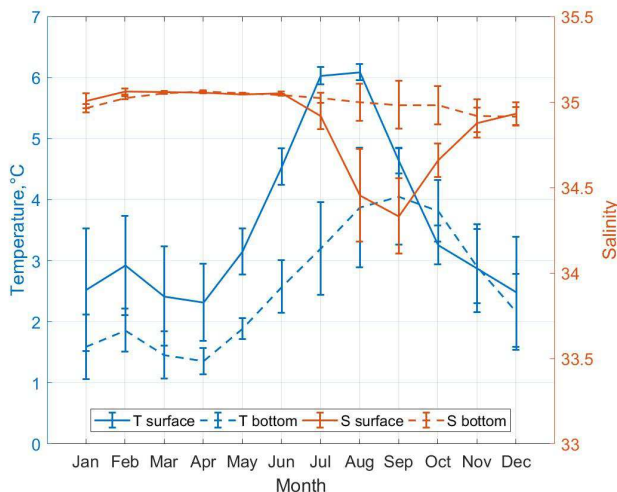
556
Figure 9. Annual cycle of bottom and surface seawater temperature and salinity in the study area,
modelled with S800-model. Lines show mean values for the study area, bars indicate spatial
variability.

3.6 Eddy driven seasonal dispersion on the shelf

Our observations indicated a large spatial variability of dissolved methane concentrations,
alongside limited vertical penetration of dissolved methane from the sources at the seafloor
towards the sea surface irrespective of vertical stratification. Based on this, we propose that
lateral advection near the seafloor plays an important role in dispersing methane horizontally
away from the seep locations. The continuous replacement of methane enriched water with water
containing low methane concentrations allows efficient dissolution of methane released in
bubbles from the sediments.

570   As shown on Fig. 6 (g-i), dissolved methane was spread horizontally in the bottom layer
571 during June-14 and July-15 while it was more concentrated around the source in May-16. The
572 water mass analysis suggests that this variability in horizontal dispersion is related to different
573 circulation patterns on the shelf. As previously discussed, circulation of waters on the shallow
574 shelf west of PKF is influenced by the combination of the WSC and superimposed local factors
575 and their seasonality. The sole presence of the AW on the shelf in June-14 for example, which led
576 to high dispersion of dissolved methane above the bottom, can be explained by an AW flooding
577 event from the WSC over the shelf (Nilsen et al., 2008; Nilsen et al., 2016). Thereby, the lateral
578 transport of waters above the PKF shelf during such flooding events disperses the dissolved
579 methane and reduces the residence time of dissolved methane above gas flares.
580   While the WSC core generally flows further offshore than the shallow PKF shelf
581 (Aagaard et al., 1987), instabilities of the WSC result in formation of numerous eddies that
582 transport AW onto the shallow shelf (Appen et al., 2016, Hattermann et al. 2016, Wekerle et al.,
583 2017). The transport occurs across the slope near the seafloor and plays an important role in the
584 exchange of AW with shelf waters in our study region (Tverberg and Nøst, 2009). We propose
585 that the observed large dispersion of dissolved methane above the bottom during the June-14
586 survey is a result of eddy activity on the shallow shelf, and that eddies play an important role in
587 the cross-frontal transport of waters and its constituents.
588   Appen et al. (2016) found increased eddy kinetic energy (EKE) and enhanced baroclinic
589 instability in the WSC in winter and spring and it is likely that this seasonality will affect the
590 number of flooding events over the shallow shelf and the residence time of methane above gas
591 flares. To investigate the relationship between the seasonality of eddy activity and the variability
592 of dissolved methane dispersion on the shelf, we used the S800-model to run numerical
593 experiments releasing and tracking particles simulating methane in our most intense flare area
594 (see Methods 2.5). The particles are freely advected by the three dimensional model velocity field
595 and provide a first order assessment of the role of the circulation in methane dispersion. The
596 buoyancy driven motion of bubbles and the aerobic oxidation of dissolved methane will add
597 further complexity to the dispersion process, but as discussed in section 3.3, are likely to be of
598 secondary importance compared to the advective controls. In the numerical experiment, we
599 observed a clear seasonality in particle dispersion with a much wider area being covered by the
600 particles from January to May as opposed to a limited area of high particle concentrations during
601 the summer months (Fig. 10).
602   During all months, the particles are mainly advected northward along the shelf and into
603 the Kongsfjorden Trough that crosses the shelf at 79° N. However, in winter and spring, the
604 pattern becomes more dispersive and particles are advected westward off the shelf, suggesting a
605 greater influence of the WSC on water mass exchange with the shallow shelf area. The residence
606 time within our study area follows the seasonal evolution of EKE (Fig 11a), with 50 % (80 %) of
607 the released particles having left the study area after 3 days (6 days) between January to April,
608 when EKE in the study area is largest. Furthermore, particles with the largest displacement (up to
609 80 – 100 km five days after the release, Fig. 11b) are associated with the highest seawater density
610 of 27.9 – 28.1 kg m^{-3}, which is consistent with the hypothesis that methane is efficiently
611 dispersed by eddies that lift dense AW onto the shelf (Tverberg and Nøst, 2009, Hattermann et al.
612 2016). Although our observations during a 3-day period in each year do not resolve the seasonal
613 cycle seen in the model, they support this principal mechanism, with the most dispersed methane
614 concentrations being observed during the June-14 and July-15 surveys when AW was present in
615 the bottom layer. Thus, our combination of observations and modelling suggests that eddies play
616 an important role in dispersing outgassing methane over the continental shelf and in controlling

617 the water column methane content, with potential direct implications for methane related
618 biogeochemical processes.
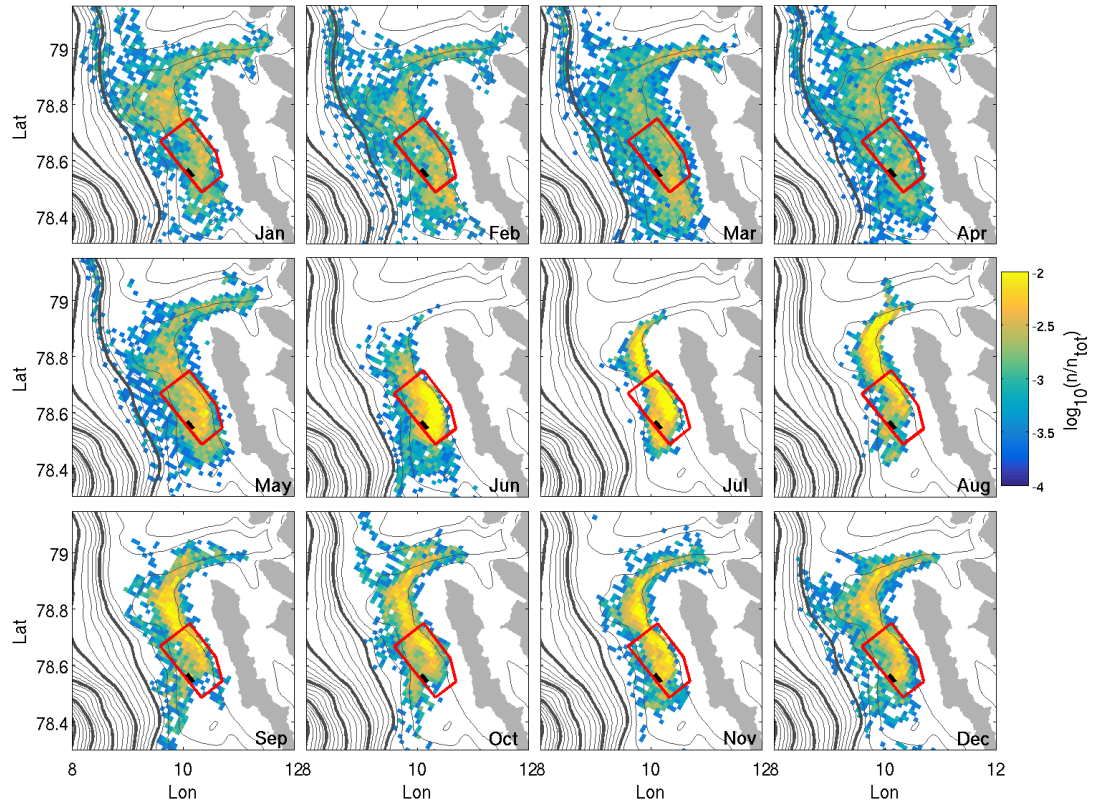
619
620 **Figure 10.** Monthly maps of particle dispersion 5 days after the particle release between 80 and
621 100 m water depth at the positions indicated by the black rectangle. Colours indicate the number
622 of particles per grid cell normalized by the total number of particles in the respective month,
623 using a logarithmic scale. The red polygon delineates the location of the sampling sites, contours
624 show the isobaths with 100 m intervals thicker lines indicating 500 m intervals.

21
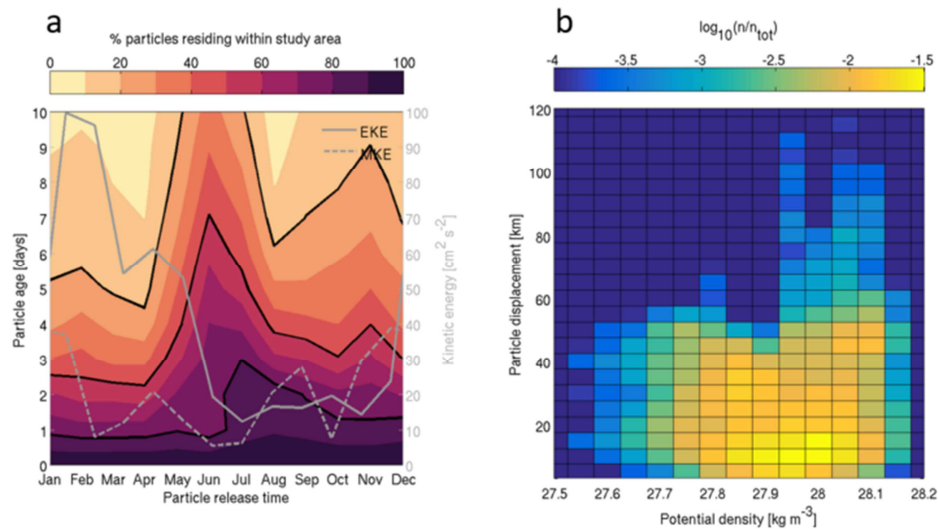
Figure 11. (**a**) Time series showing the residence time of particles within the study area indicated by the red polygon in Fig. 10 (colour shade), together with monthly averaged mean- (MKE) and eddy (EKE) kinetic energy (right axis), averaged for the same region. Black curves indicate times when 20 %, 50 % and 80 % of particles have left the study area. (**b**) Two-dimensional histogram of particle displacement vs. potential density at the particle position after five days. Colours indicate the normalized frequency of occurrence on a logarithmic scale, showing that many particles remains within 20 km of the source and that the largest displacements are associated with the highest densities.

4 Conclusions

To our knowledge, this is the first study of the water column above cold methane seeps that combines a multiyear series of oceanographic surveys with stations positioned on a grid within a defined polygon. This study clearly benefits from the grid station design when compared to more frequently conducted single synoptic transects. Acquiring data in a four dimensional array in time and space allowed us to evaluate the methane content in the entire water body above methane flares and clearly identify the major processes mediating water column methane content and transport.

Our results suggest the possibility of enhanced methane flux from the sediments triggered by elevated bottom water temperature in the absence of underlying gas hydrate. In light of warming waters of the Arctic Ocean, not only gas hydrate containing sediments, but all methane gas bearing sediments could potentially become sources of methane release into the water column. Further study of the processes involved and the links between gas bearing sediments and bottom water temperature is required to improve our understanding.

Comparison between the three different hydrographic regimes observed across the three surveys reveals that most of the released methane in our shallow shelf area remains in the bottom and intermediate waters irrespective of the strength of stratification. Therefore, hypotheses by e.g. Schneider von Deimling et al., (2011), who suggested that all methane could be liberated to the atmosphere from shallow shelf areas as a result of a well-mixed water column and absence of

22

653 stratification appear not to be valid in our shallow shelf study area. Small amounts of methane
654 could be liberated to the atmosphere, but mainly as a result of strong winds increasing the rate of
655 air-sea gas exchange, not weak stratification.

656   As expected, we find the horizontal advection to be the main mechanism controlling the
657 dispersion of dissolved methane on the Prins Karls Forland shelf instead of vertical transport. In
658 particular, our results highlight the role of mesoscale eddies in controlling the methane content
659 above, dispersion around, and displacement away from gas flares. This implies that eddies and
660 horizontal dispersion may also have important effects on methane related biogeochemical process
661 and the magnitude of different methane sinks. For example, one could anticipate that a potential
662 for methane sink through MOx could be higher when eddy activity is high in winter and spring
663 season, because by dispersing dissolved methane over a larger area, eddies promote delivery of
664 dissolved methane to methane oxidizing bacteria that consequently capture and consume this
665 methane. Further seasonal measurements and/or process oriented modelling will be required to
666 scrutinize these ideas, but these results could considerably shift our understanding of the
667 seasonality of sinks of dissolved methane and allow better estimates of the balance between
668 amounts of methane released from sediments, methane liberated into the atmosphere, and
669 methane removed from the system through microbial processes.

670 **Acknowledgements**

684

685   **References**

686   Aagaard, K., Foldvik, A., & Hillman, S. (1987). The West Spitsbergen Current: disposition and
687   water mass transformation. *Journal of Geophysical Research: Oceans, 92*(C4), 3778-
688   3784.
689   Albretsen, J., Hattermann, T., & Sundfjord, A. (2017). Ocean and sea ice circulation model
690   results from Svalbard area (ROMS) [Data set]. Norwegian Polar Institute.
691   Amante, C. (2009). ETOPO1 1 arc-minute global relief model: procedures, data sources and
692   analysis. *http://www. ngdc. noaa. gov/mgg/global/global. html*.
693   Andreassen, K., Hubbard, A., Winsborrow, M., Patton, H., Vadakkepuliyambatta, S., Plaza-
694   Faverola, A., . . . Mattingsdal, R. (2017). Massive blow-out craters formed by hydrate-
695   controlled methane expulsion from the Arctic seafloor. *Science, 356*(6341), 948-953.
696   Appen, W.-J. v., Schauer, U., Hattermann, T., & Beszczynska-Möller, A. (2016). Seasonal cycle
697   of mesoscale instability of the West Spitsbergen Current. *Journal of Physical
698   Oceanography, 46*(4), 1231-1254.
699   Berge, J., Johnsen, G., Nilsen, F., Gulliksen, B., & Slagstad, D. (2005). Ocean temperature
700   oscillations enable reappearance of blue mussels Mytilus edulis in Svalbard after a 1000
701   year absence. *Marine Ecology Progress Series, 303*, 167-175.
702   Berndt, C., Feseker, T., Treude, T., Krastel, S., Liebetrau, V., Niemann, H., . . . Ferré, B. (2014).
703   Temporal constraints on hydrate-controlled methane seepage off Svalbard. *Science,
704   343*(6168), 284-287.
705   Beszczynska-Möller, A., Fahrbach, E., Schauer, U., & Hansen, E. (2012). Variability in Atlantic
706   water temperature and transport at the entrance to the Arctic Ocean, 1997–2010. *ICES
707   Journal of Marine Science, 69*(5), 852-863.
708   Budgell, W. (2005). Numerical simulation of ice-ocean variability in the Barents Sea region.
709   *Ocean Dynamics, 55*(3-4), 370-387.
710   Cottier, F., Nilsen, F., Inall, M., Gerland, S., Tverberg, V., & Svendsen, H. (2007). Wintertime
711   warming of an Arctic shelf in response to large☐scale atmospheric circulation.
712   *Geophysical Research Letters, 34*(10).
713   Cottier, F., Tverberg, V., Inall, M., Svendsen, H., Nilsen, F., & Griffiths, C. (2005). Water mass
714   modification in an Arctic fjord through cross☐shelf exchange: The seasonal hydrography
715   of Kongsfjorden, Svalbard. *Journal of Geophysical Research: Oceans, 110*(C12).
716   Cottier, F. R., Nilsen, F., Skogseth, R., Tverberg, V., Skarðhamar, J., & Svendsen, H. (2010).
717   Arctic fjords: a review of the oceanographic environment and dominant physical
718   processes. *Geological Society, London, Special Publications, 344*(1), 35-50.
719   Crews, L., Sundfjord, A., Albretsen, J., & Hattermann, T. (2018). Mesoscale eddy activity and
720   transport in the Atlantic Water inflow region north of Svalbard. *Journal of Geophysical
721   Research: Oceans, 123*(1), 201-215.
722   Damm, E., Mackensen, A., Budéus, G., Faber, E., & Hanfland, C. (2005). Pathways of methane
723   in seawater: Plume spreading in an Arctic shelf environment (SW-Spitsbergen).
724   *Continental Shelf Research, 25*(12), 1453-1472.
725   Damm, E., Thoms, S., Beszczynska-Möller, A., Nöthig, E.-M., & Kattner, G. (2015). Methane
726   excess production in oxygen-rich polar water and a model of cellular conditions for this
727   paradox. *Polar Science, 9*(3), 327-334.

728 Dee, D. P., Uppala, S., Simmons, A., Berrisford, P., Poli, P., Kobayashi, S., . . . Bauer, P. (2011).
729   The ERA☐Interim reanalysis: Configuration and performance of the data assimilation
730   system. *Quarterly Journal of the royal meteorological society, 137*(656), 553-597.
731 Döös, K., Jönsson, B., & Kjellsson, J. (2017). Evaluation of oceanic and atmospheric trajectory
732   schemes in the TRACMASS trajectory model v6. 0. *Geoscientific Model*
733   *Development*, *10*(4), 1733.
734 Ferré, B., Mienert, J., & Feseker, T. (2012). Ocean temperature variability for the past 60 years
735   on the Norwegian☐Svalbard margin influences gas hydrate stability on human time
736   scales. *Journal of Geophysical Research: Oceans, 117*(C10).
737 Fofonoff, N. P., & Millard Jr, R. (1983). Algorithms for the computation of fundamental
738   properties of seawater.
739 Gentz, T., Damm, E., von Deimling, J. S., Mau, S., McGinnis, D. F., & Schlüter, M. (2014). A
740   water column study of methane around gas flares located at the West Spitsbergen
741   continental margin. *Continental Shelf Research, 72*, 107-118.
742 Graversen, R. G., Mauritsen, T., Tjernström, M., Källén, E., & Svensson, G. (2008). Vertical
743   structure of recent Arctic warming. *Nature, 451*(7174), 53.
744 Graves, C. A., Steinle, L., Rehder, G., Niemann, H., Connelly, D. P., Lowry, D., . . . James, R. H.
745   (2015). Fluxes and fate of dissolved methane released at the seafloor at the landward limit
746   of the gas hydrate stability zone offshore western Svalbard. *Journal of Geophysical*
747   *Research: Oceans, 120*(9), 6185-6201.
748 Greinert, J., Artemov, Y., Egorov, V., De Batist, M., & McGinnis, D. (2006). 1300-m-high rising
749   bubbles from mud volcanoes at 2080 m in the Black Sea: Hydroacoustic characteristics
750   and temporal variability. *Earth and Planetary Science Letters, 244*(1-2), 1-15.
751 Hanson, R. S., & Hanson, T. E. (1996). Methanotrophic bacteria. *Microbiological reviews, 60*(2),
752   439-471.
753 Hattermann, T., Isachsen, P. E., Appen, W. J., Albretsen, J., & Sundfjord, A. (2016). Eddy☐
754   driven recirculation of Atlantic Water in Fram Strait. *Geophysical Research Letters,*
755   *43*(7), 3406-3414.
756 Hester, K. C., & Brewer, P. G. (2009). Clathrate hydrates in nature. *Annual review of marine*
757   *science, 1*, 303-327.
758 Hsu, S., Meindl, E. A., & Gilhousen, D. B. (1994). Determining the power-law wind-profile
759   exponent under near-neutral stability conditions at sea. *Journal of Applied Meteorology,*
760   *33*(6), 757-765.
761 Jakobsson, M., Mayer, L., Coakley, B., Dowdeswell, J. A., Forbes, S., Fridman, B., . . . Rebesco,
762   M. (2012). The international bathymetric chart of the Arctic Ocean (IBCAO) version 3.0.
763   *Geophysical Research Letters, 39*(12).
764 James, R. H., Bousquet, P., Bussmann, I., Haeckel, M., Kipfer, R., Leifer, I., . . . Rehder, G.
765   (2016). Effects of climate change on methane emissions from seafloor sediments in the
766   Arctic Ocean: A review. *Limnology and Oceanography, 61*(S1).
767 Kannberg, P. K., Tréhu, A. M., Pierce, S. D., Paull, C. K., & Caress, D. W. (2013). Temporal
768   variation of methane flares in the ocean above Hydrate Ridge, Oregon. *Earth and*
769   *Planetary Science Letters, 368*, 33-42.
770 Karl, D. M., Beversdorf, L., Björkman, K. M., Church, M. J., Martinez, A., & Delong, E. F.
771   (2008). Aerobic production of methane in the sea. *Nature Geoscience, 1*(7), 473.
772 Kessler, J. D., Valentine, D. L., Redmond, M. C., Du, M., Chan, E. W., Mendes, S. D., . . .
773   Werra, L. M. (2011). A persistent oxygen anomaly reveals the fate of spilled methane in
774   the deep Gulf of Mexico. *Science, 331*(6015), 312-315.

775 Knies, J., Damm, E., Gutt, J., Mann, U., & Pinturier, L. (2004). Near☐surface hydrocarbon
776   anomalies in shelf sediments off Spitsbergen: Evidences for past seepages. *Geochemistry,*
777   *Geophysics, Geosystems, 5*(6).
778 Kort, E., Wofsy, S., Daube, B., Diao, M., Elkins, J., Gao, R., . . . Moore, F. (2012). Atmospheric
779   observations of Arctic Ocean methane emissions up to 82 north. *Nature Geoscience, 5*(5),
780   318.
781 Kretschmer, K., Biastoch, A., Rüpke, L., & Burwicz, E. (2015). Modeling the fate of methane
782   hydrates under global warming. *Global Biogeochemical Cycles, 29*(5), 610-625.
783 Kvenvolden, K. A., Lilley, M. D., Lorenson, T. D., Barnes, P. W., & McLaughlin, E. (1993). The
784   Beaufort Sea continental shelf as a seasonal source of atmospheric methane. *Geophysical*
785   *Research Letters, 20*(22), 2459-2462.
786 Lammers, S., Suess, E., & Hovland, M. (1995). A large methane plume east of Bear Island
787   (Barents Sea): implications for the marine methane cycle. *Geologische Rundschau, 84*(1),
788   59-66.
789 LANDVIK, J. Y., Ingolfsson, O., MIENERT, J., LEHMAN, S. J., Solheim, A., ELVERHØI, A.,
790   & Ottesen, D. (2005). Rethinking Late Weichselian ice☐sheet dynamics in coastal NW
791   Svalbard. *Boreas, 34*(1), 7-24.
792 Leifer, I., Jeuthe, H., Gjøsund, S. H., & Johansen, V. (2009). Engineered and natural marine seep,
793   bubble-driven buoyancy flows. *Journal of Physical Oceanography, 39*(12), 3071-3090.
794 Marín☐Moreno, H., Minshull, T. A., Westbrook, G. K., & Sinha, B. (2015). Estimates of future
795   warming☐induced methane emissions from hydrate offshore west Svalbard for a range of
796   climate models. *Geochemistry, Geophysics, Geosystems, 16*(5), 1307-1323.
797 Mau, S., Römer, M., Torres, M. E., Bussmann, I., Pape, T., Damm, E., . . . Loher, M. (2017).
798   Widespread methane seepage along the continental margin off Svalbard-from Bjørnøya to
799   Kongsfjorden. *Scientific reports, 7*, 42997.
800 McGinnis, D. F., Greinert, J., Artemov, Y., Beaubien, S., & Wüest, A. (2006). Fate of rising
801   methane bubbles in stratified waters: How much methane reaches the atmosphere?
802   *Journal of Geophysical Research: Oceans, 111*(C9).
803 Millard, R., Owens, W., & Fofonoff, N. (1990). On the calculation of the Brunt-Väisälä
804   frequency. *Deep Sea Research Part A. Oceanographic Research Papers, 37*(1), 167-181.
805 Myhre, C. L., Ferré, B., Platt, S. M., Silyakova, A., Hermansen, O., Allen, G., . . . Pitt, J. (2016).
806   Extensive release of methane from Arctic seabed west of Svalbard during summer 2014
807   does not influence the atmosphere. *Geophysical Research Letters, 43*(9), 4624-4631.
808 Nikolovska, A., Sahling, H., & Bohrmann, G. (2008). Hydroacoustic methodology for detection,
809   localization, and quantification of gas bubbles rising from the seafloor at gas seeps from
810   the eastern Black Sea. *Geochemistry, Geophysics, Geosystems, 9*(10).
811 Nilsen, F., Cottier, F., Skogseth, R., & Mattsson, S. (2008). Fjord–shelf exchanges controlled by
812   ice and brine production: the interannual variation of Atlantic Water in Isfjorden,
813   Svalbard. *Continental Shelf Research, 28*(14), 1838-1853.
814 Nilsen, F., Skogseth, R., Vaardal-Lunde, J., & Inall, M. (2016). A simple shelf circulation model:
815   Intrusion of Atlantic water on the West Spitsbergen shelf. *Journal of Physical*
816   *Oceanography, 46*(4), 1209-1230.
817 Ostrovsky, I., McGinnis, D. F., Lapidus, L., & Eckert, W. (2008). Quantifying gas ebullition with
818   echosounder: the role of methane transport by bubbles in a medium☐sized lake.
819   *Limnology and Oceanography: Methods, 6*(2), 105-118.

Parmentier, F.-J. W., Silyakova, A., Biastoch, A., Kretschmer, K., & Panieri, G. (2015). Natural marine methane sources in the Arctic. In: *Arctic Monitoring and Assessment Programme (AMAP)*.

Paull, C. K., Ussler, W., Dallimore, S. R., Blasco, S. M., Lorenson, T. D., Melling, H., . . . McLaughlin, F. A. (2007). Origin of pingo□like features on the Beaufort Sea shelf and their possible relationship to decomposing methane gas hydrates. *Geophysical Research Letters, 34*(1).

Perkin, R., & Lewis, E. (1984). Mixing in the West Spitsbergen current. *Journal of Physical Oceanography, 14*(8), 1315-1325.

Pierrot, D., Neill, C., Sullivan, K., Castle, R., Wanninkhof, R., Lüger, H., . . . Cosca, C. E. (2009). Recommendations for autonomous underway pCO2 measuring systems and data-reduction routines. *Deep Sea Research Part II: Topical Studies in Oceanography, 56*(8-10), 512-522.

Polyakov, I., Alekseev, G., Timokhov, L., Bhatt, U., Colony, R., Simmons, H., . . . Zakharov, V. (2004). Variability of the intermediate Atlantic water of the Arctic Ocean over the last 100 years. *Journal of Climate, 17*(23), 4485-4497.

Polyakov, I., Timokhov, L., Dmitrenko, I., Ivanov, V., Simmons, H., Beszczynska□Möller, A., . . . Gascard, J. C. (2007). Observational program tracks Arctic Ocean transition to a warmer state. *Eos, Transactions American Geophysical Union, 88*(40), 398-399.

Polyakov, I. V., Timokhov, L. A., Alexeev, V. A., Bacon, S., Dmitrenko, I. A., Fortier, L., . . . Ivanov, V. V. (2010). Arctic Ocean warming contributes to reduced polar ice cap. *Journal of Physical Oceanography, 40*(12), 2743-2756.

Portnov, A., Smith, A. J., Mienert, J., Cherkashov, G., Rekant, P., Semenov, P., . . . Vanshtein, B. (2013). Offshore permafrost decay and massive seabed methane escape in water depths> 20 m at the South Kara Sea shelf. *Geophysical Research Letters, 40*(15), 3962-3967.

Portnov, A., Vadakkepuliyambatta, S., Mienert, J., & Hubbard, A. (2016). Ice-sheet-driven methane storage and release in the Arctic. *Nature communications, 7*, 10314.

Reeburgh, W. S. (2007). Oceanic methane biogeochemistry. *Chemical reviews, 107*(2), 486-513.

Römer, M., Riedel, M., Scherwath, M., Heesemann, M., & Spence, G. D. (2016). Tidally controlled gas bubble emissions: A comprehensive study using long□term monitoring data from the NEPTUNE cabled observatory offshore Vancouver Island. *Geochemistry, Geophysics, Geosystems, 17*(9), 3797-3814.

Rudels, B., Jones, E., Anderson, L., & Kattner, G. (1994). On the intermediate depth waters of the Arctic Ocean. *The polar oceans and their role in shaping the global environment*, 33-46.

Sahling, H., Römer, M., Pape, T., Bergès, B., dos Santos Fereirra, C., Boelmann, J., . . . Dimmler, W. (2014). Gas emissions at the continental margin west of Svalbard: mapping, sampling, and quantification. *Biogeosciences, 11*(21), 6029.

Sarkar, S., Berndt, C., Minshull, T. A., Westbrook, G. K., Klaeschen, D., Masson, D. G., . . . Thatcher, K. E. (2012). Seismic evidence for shallow gas□escape features associated with a retreating gas hydrate zone offshore west Svalbard. *Journal of Geophysical Research: Solid Earth, 117*(B9).

Schmale, O., Greinert, J., & Rehder, G. (2005). Methane emission from high□intensity marine gas seeps in the Black Sea into the atmosphere. *Geophysical Research Letters, 32*(7).

Serov, P., Portnov, A., Mienert, J., Semenov, P., & Ilatovskaya, P. (2015). Methane release from pingo□like features across the South Kara Sea shelf, an area of thawing offshore permafrost. *Journal of Geophysical Research: Earth Surface, 120*(8), 1515-1529.

867   Serov, P., Vadakkepuliyambatta, S., Mienert, J., Patton, H., Portnov, A., Silyakova, A., . . .
868   Andreassen, K. (2017). Postglacial response of Arctic Ocean gas hydrates to climatic
869   amelioration. *Proceedings of the National Academy of Sciences*, 201619288.
870   Serreze, M. C., & Francis, J. A. (2006). The Arctic amplification debate. *Climatic change, 76*(3-
871   4), 241-264.
872   Shakhova, N., Semiletov, I., Leifer, I., Sergienko, V., Salyuk, A., Kosmach, D., . . . Tumskoy, V.
873   (2013). Ebullition and storm-induced methane release from the East Siberian Arctic Shelf.
874   *Nature Geoscience, 7*(1), ngeo2007.
875   Shakhova, N., Semiletov, I., Salyuk, A., Yusupov, V., Kosmach, D., & Gustafsson, Ö. (2010).
876   Extensive methane venting to the atmosphere from sediments of the East Siberian Arctic
877   Shelf. *Science, 327*(5970), 1246-1250.
878   Shchepetkin, A. F., & McWilliams, J. C. (2005). The regional oceanic modeling system (ROMS):
879   a split-explicit, free-surface, topography-following-coordinate oceanic model. *Ocean
880   modelling, 9*(4), 347-404.
881   Smith, A. J., Mienert, J., Bünz, S., & Greinert, J. (2014). Thermogenic methane injection via
882   bubble transport into the upper Arctic Ocean from the hydrate☐charged Vestnesa Ridge,
883   Svalbard. *Geochemistry, Geophysics, Geosystems, 15*(5), 1945-1959.
884   Soreide, N. N., Jeffries, M., Richter-Menge, J., & Overland, J. (2016). The Arctic Report Card.
885   *Bulletin of the American Meteorological Society, 97*(8), 1339-1341.
886   Steinle, L., Graves, C. A., Treude, T., Ferré, B., Biastoch, A., Bussmann, I., . . . Behrens, E.
887   (2015). Water column methanotrophy controlled by a rapid oceanographic switch. *Nature
888   Geoscience, 8*(5), 378.
889   Storkey, D., Blockley, E., Furner, R., Guiavarc'h, C., Lea, D., Martin, M., . . . Siddorn, J. (2010).
890   Forecasting the ocean state using NEMO: The new FOAM system. *Journal of operational
891   oceanography, 3*(1), 3-15.
892   Teigen, S. H., Nilsen, F., & Gjevik, B. (2010). Barotropic instability in the West Spitsbergen
893   Current. *Journal of Geophysical Research: Oceans, 115*(C7).
894   Tverberg, V., & Nøst, O. (2009). Eddy overturning across a shelf edge front: Kongsfjorden, west
895   Spitsbergen. *Journal of Geophysical Research: Oceans, 114*(C4).
896   Veloso, M., Greinert, J., Mienert, J., & De Batist, M. (2015). A new methodology for quantifying
897   bubble flow rates in deep water using splitbeam echosounders: Examples from the Arctic
898   offshore NW☐Svalbard. *Limnology and Oceanography: Methods, 13*(6), 267-287.
899   von Deimling, J. S., Rehder, G., Greinert, J., McGinnnis, D., Boetius, A., & Linke, P. (2011).
900   Quantification of seep-related methane gas emissions at Tommeliten, North Sea.
901   *Continental Shelf Research, 31*(7-8), 867-878.
902   Wallmann, K., Riedel, M., Hong, W., Patton, H., Hubbard, A., Pape, T., . . . Torres, M. (2018).
903   Gas hydrate dissociation off Svalbard induced by isostatic rebound rather than global
904   warming. *Nature communications, 9*(1), 83.
905   Wanninkhof, R., Asher, W. E., Ho, D. T., Sweeney, C., & McGillis, W. R. (2009). Advances in
906   quantifying air-sea gas exchange and environmental forcing.
907   Weiss, R., & Price, B. (1980). Nitrous oxide solubility in water and seawater. *Marine chemistry,
908   8*(4), 347-359.
909   Wekerle, C., Wang, Q., von Appen, W. J., Danilov, S., Schourup-Kristensen, V., & Jung, T.
910   (2017). Eddy☐Resolving Simulation of the Atlantic Water Circulation in the Fram Strait
911   With Focus on the Seasonal Cycle. *Journal of Geophysical Research: Oceans, 122*(11),
912   8385-8405.

913   Westbrook, G. K., Thatcher, K. E., Rohling, E. J., Piotrowski, A. M., Pälike, H., Osborne, A. H., .
914   . . James, R. H. (2009). Escape of methane gas from the seabed along the West
915   Spitsbergen continental margin. *Geophysical Research Letters, 36*(15).
916   Wiesenburg, D. A., & Guinasso Jr, N. L. (1979). Equilibrium solubilities of methane, carbon
917   monoxide, and hydrogen in water and sea water. *Journal of Chemical and Engineering*
918   *Data, 24*(4), 356-360.
919

920 **Supplementary material**
921
922 **Content**
923
924 Text S1 to S2
925 Figures S1 to S3

926 **Introduction**

927 Supporting Text S1 and Figure S1 provide details of the method of scaling up gas flow rate estimates to
928 the entire study area.

929 Supporting Text S2 and Figure S2 provide a detailed description of the water column methane content
930 calculations in different layers.

931 Supporting Figure S3 shows additional information on bottom water temperature to support the main text
932 in Results and Discussion section 3.1.

933 **Text S1. Method for scaling up the flow rates**

934

935 Because the fraction of the study area covered by the echosounder was small and slightly different
936 between the three surveys, we applied a scaling up procedure including a Kriging interpolation to facilitate
937 comparison between surveys (Figure S1). The entire area was gridded into cells of 100×100 m, and, as a
938 result three types of cells were considered: 1) completely covered, 2) partly covered or 3) not covered by
939 the echosounder beam footprint. For each cell, we estimated methane flow rates: (a) If one or several
940 flares were detected within cell type 1, the estimated flow rate was applied for the entire cell area. (b) In
941 the absence of flares in cell type 1, the flow rate was set to zero. (c) If one or several flares were within
942 cell type 2, the sum of the flow rates within the cell was normalized by the fraction of the cell covered by
943 the beam footprint. (d) In the absence of flares in cell type 2, the flow rate was set to zero. (e) For cell type
944 3, (no data acquired) we interpolated flow rates from neighbouring cells. In order to find a smooth and
945 plausible flowrate distribution, a 3x3 low-pass filter and the Kriging interpolation method embedded in
946 ArcGIS was applied. Finally, to calculate the mean flux (mol m^{-2} s^{-1}) in the entire area, the sum of the
947 scaled up flow rates were normalized by the survey area (Table 1).

948

949 **Text S2. Calculation of methane content in the water column**
950
951 Methane content in the water column was calculated by integrating distinct methane concentration values
952 over depth. For this approach, we approximated the definite integral linearly by applying the trapezoid
953 rule. For each discrete sampling point shown on Fig. S2, we had a corresponding depth (Z, m) and CH_4
954 concentration (C, nmol L^{-1}). To determine the vertically integrated methane content (C_{int}) for every depth
955 (meter) of water column between sampling points (nmol L^{-1} m) we interpolated linearly as follows:
956
957 $C_{int}=(CS_1+CS_2)/2*(ZS_2-ZS_1)$ (Eq. SI1)
958
959 We then summed all C_{int} in each layer and multiplied by 10^3 to obtain methane content per m^2 in every
960 layer (nmol m^{-2}) for each of the CTD stations.
961
962 To account for spatial sampling irregularity between CTD stations, we determined the area-weighted
963 average of the CH_4 content for each layer. For this, we created a grid between longitudes 9.5° E and 10.8°
964 E and latitudes 78.4° N and 78.7° N with bin sizes of $0.01 \times 0.01°$ in both directions. The resulting grid
965 included 101×201 points. We then projected C_{int} for each layer and station onto this grid using the Matlab
966 function griddata for horizontal interpolation. Finally, we calculated the area-weighted average using the
967 Matlab function mean2 of the gridded data. Then we scaled up (multiplied) the area-weighted averages for
968 each layer to the size of the investigated area (423 km^2), yielding the total methane content (in mol) for
969 each layer.
970
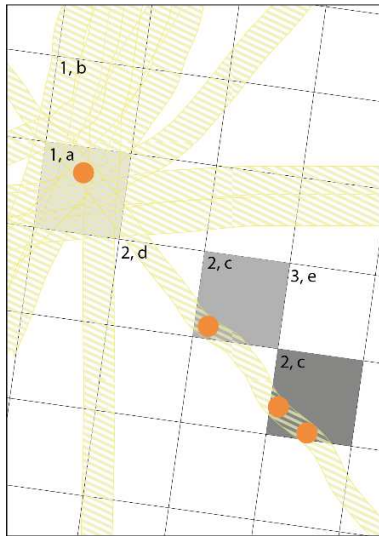
971
972 **Figure S1.** Schematic of flowrate interpolation. Squares indicate 100x100 meter grid cells where the
973 darkness indicates the relative summed flow rates within each cell. Yellow-hashed areas indicate the
974 echosounder beam coverage and dots indicate flares. Cell types 1 – 3 and interpolation schemes a – e are
975 described in the text S1.
976
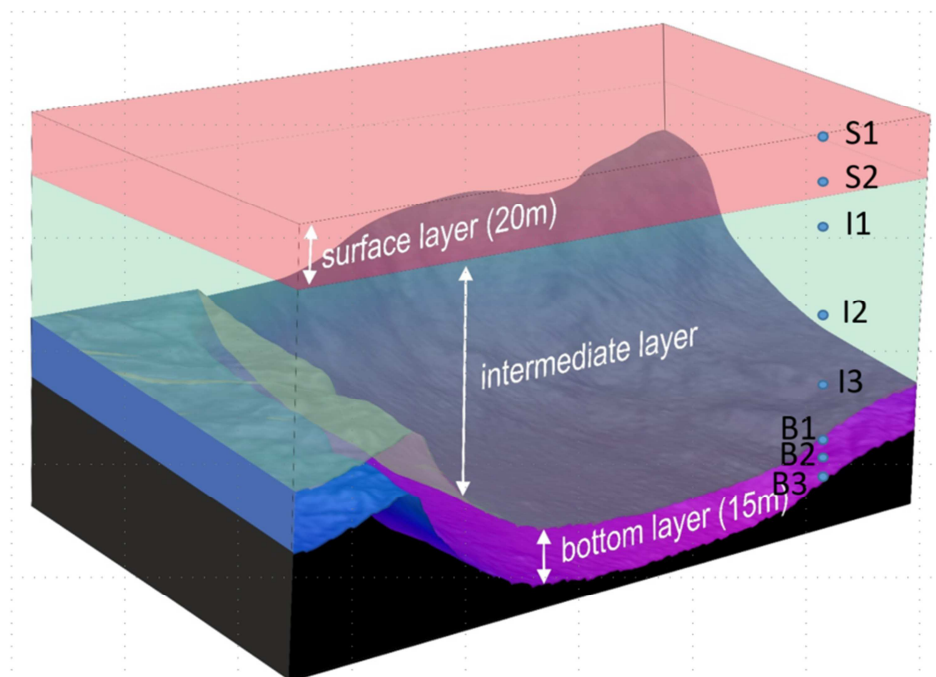
977
978 **Figure S2.** Schematic shows the bottom layer (0-15 meters above seafloor), the intermediate layer (15
979 meters above seafloor to 20 m water depth) and the surface layer (20 m water depth to sea surface). The
980 blue dots show discrete sampling points in the surface (S1, S2), intermediate (I1, I2, I3) and bottom (B1,
981 B2, B3) layer.
982
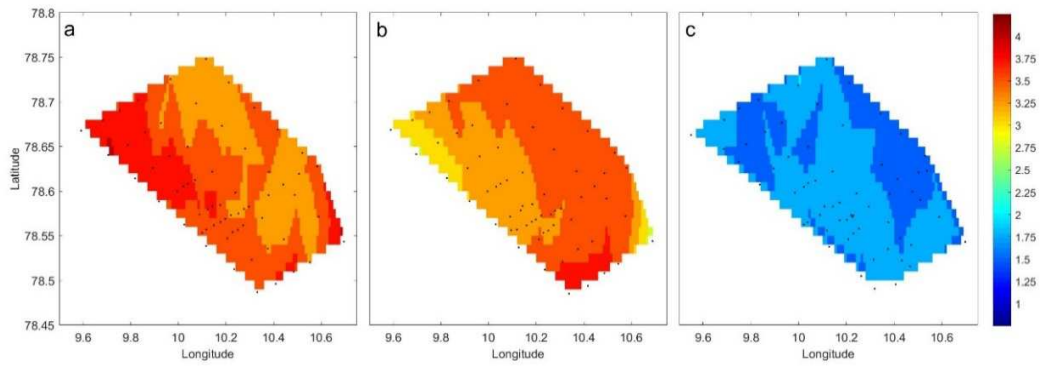
983
984 **Figure S3.** Bottom water temperature during the June-14 (**a**), July-15 (**b**) and May-16 (**c**) surveys.
985

Highlights

- Gas seepage intensity and lateral water mass movements are key controls of water column methane content

- Vertical methane transport is limited irrespective of stratification

- Eddies play a key role in horizontal advection and dispersion of dissolved methane

Conflict of Interest Statement

The authors declare that they have no known competing financial interests or personal relationships that could have appeared to influence the work reported in this paper.